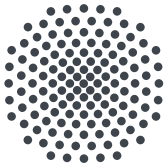

University of Stuttgart
5th Physics Institute

Vorgelegt an der Universität Stuttgart

Master's Thesis

Towards a high repetition single-photon source using a Rydberg blockade in a vapor cell

Annika Belz

August 10, 2021

Examiner: Prof. Dr. Tilman Pfau
2nd Examiner: Prof. Dr. Hidenori Takagi

Ehrenwörtliche Erklärung

Ich erkläre hiermit, dass ich die vorliegende Arbeit selbständig verfasst, nur unter Verwendung der angegebenen Quellen und Hilfsmittel angefertigt habe und alle wörtlich oder sinngemäß aus anderen Werken übernommenen Aussagen als solche gekennzeichnet sind. Die vorliegende Arbeit war weder vollständig noch in Teilen Gegenstand eines anderen Prüfungsverfahrens. Weiterhin stimmt das elektronische Exemplar mit der gedruckten Version überein.

Stuttgart, den 10. August 2021

Annika Belz

Zusammenfassung

Die aktuell große Popularität von Quantencomputern sorgt auch für ein erhöhtes Interesse an den damit verbundenen Schlüsseltechnologien. Die Funktionsweise eines Quantencomputers basiert auf nicht binären Quanten-Bits (Qubits), welche als quantenmechanisches zwei-Niveau System realisiert werden können. Ein Ansatz basiert einzig auf linear-optischen Komponenten wie Strahlteilern und Verzögerungsplättchen. In einem solchen System wird das Qubit als die Polarisation einzelner Photonen realisiert, wobei, neben weiteren Bauteilen, eine parametrische Einzelphotonenquelle benötigt wird.
Ein Ansatz zu deren Realisierung basiert auf Rydbergatomen. Dies sind Atome mit mindestens einem Elektron in einem Zustand mit hoher Hauptquantenzahl. Der große Abstand zwischen Rumpfelektronen und Rydbergelektron und dessen daraus resultierender schwacher Bindung, sorgt für eine erhöhte Empfindlichkeit gegenüber elektromagnetischen Feldern. Dies führt zur Rydbergblockade, einem kollektiven Effekt der pro Blockadevolumen nur ein Atom im Rydbergzustand zulässt.
In unserer Gruppe wurde die Machbarkeit einer Einzelphotonenquelle basierend auf Rydbergblockade und gepulstem Vier-Wellen-Mischen mit Rubidium bei Raumtemperatur demonstriert. Aufgrund von technischen Limitierungen bei Anregung über die $5P_{1/2}$ bzw. $5P_{3/2}$ Zwischenniveaus konnte nur eine Photonenausbeute von 4 % erreicht werden. Um diese zu verbessern, kann ein anderes Anregungsschema mit $6P_{1/2}$ und $6P_{3/2}$ als Zwischenniveaus verwendet werden.
Im Rahmen dieser Arbeit wurden erste systematische Messungen zur Anregung in den Rydbergzustand in diesem invertierten Levelschema durchgeführt.
Im ersten Teil wurden dazu Dauerstrichlaser verwendet, wobei zunächst eine Autler-Townes Aufspaltung untersucht wurde. Simulationen eines Dreiniveausystems im Gleichgewichtszustand bestätigen diese Messungen quantitativ und qualitativ. Weiterhin wurden Elektromagnetisch induzierte Transparenz sowie der Übergang zu induzierter Absorption beobachtet.
Im zweiten Teil wurde ein gepulster Faserverstärker verwendet um Nanosekundenpulse mit Spitzenleistungen von bis zu 100 W für den Rydbergübergang zu erzeugen. Durch stärkeres Fokussieren konnten so Rabi-Frequenzen von bis zu einem Gigahertz erreicht werden. Diese Oszillationen konnten direkt gemessen werden und sind in guter Übereinstimmung mit zugehörigen Simulationen eines Dreiniveausystems.
Bei Untersuchungen zum Verhalten bei zusätzlicher Verstimmung des Rydberglasers war das Experiments nicht derartig zu reproduzieren, was den Rückschluss auf weitere Prozesse, wie die Entstehung eines Plasmas zulässt.
Um den Ursprung für diese Diskrepanzen nachzuvollziehen sind weitere, systematische Messungen, zum Beispiel im Rahmen verstimmungsaufgelöster Messreihen für beide beteiligte Laser notwendig.

Contents

Introduction

The current omnipresent interest in quantum computers is creating a great demand for the associated key-technologies. The working principle of a quantum computer is based on non-binary quantum bits (qubits), which can be implemented as a two-level quantum mechanical system. One possible approach relies solely on linear optical elements, like beam splitters and phase shifters [1]. In those systems the qubit is encoded as the polarization of single photons, which requires, among other components, on-demand single-photon sources.

Such single-photon sources can be realized through different solid-state effects e.g. by embedding quantum dots into semiconductors [2] or color centers into diamond [3]. Due to additional noise in solids caused by e.g. phonons, the spectral stability and phase noise of the emitted photons is inherently limited. Atoms on the other hand, emit identical photons possibly only restricted by the time bandwidth product.

One approach to create single photons employs Rydberg atoms [4]. Those have at least one electron excited to a state with high principle quantum number. Due to the large distance between the core electrons and the Rydberg electron and its subsequently weak binding, such atoms are highly sensitive towards external electromagnetic fields including other Rydberg atoms. This leads to the Rydberg blockade [5], describing the collective effect of only a single allowed excitation to the Rydberg state per blockade volume.

Our research group demonstrated [6] a room-temperature on-demand single-photon source using rubidium by combining the Rydberg blockade effect and a pulsed four-wave mixing process. However, this experiment suffered from a mean generation efficiency of only 4 % and a low repetition rate of 50 Hz. The main limiting factors were the home-made dye amplifiers at a fundamentally hard to amplify wavelength of 480 nm between the $5P_{1/2}$ and $5P_{3/2}$ intermediate state and the Rydberg level. In order to improve these issues, a different excitation scheme using the $6P_{1/2}$ and $6P_{3/2}$ intermediate states can be employed.

In the frame of this thesis, first systematic measurements investigating the pulsed two photon excitation in rubidium using this inverted level scheme were performed.

As a first step, these were done using continuous wave lasers. In the resulting steady state regime, Autler-Townes splitting, electromagnetically induced transparency, enhanced absorption and the smooth transition between these effects could be observed.

Subsequently, a customized Yb-doped fiber amplifier [7], creating nanosecond pulses with a peak power of up to 100 W, was used to drive the Rydberg transition. Rabi oscillations between the $6P_{1/2}$ and Rydberg state with oscillation frequencies of up to $1 \cdot 2\pi$ GHz were directly measured. These observations in the inverted scheme show fully coherent dynamics involving a Rydberg state above room temperature in a millimeter cell.

Part I

Theoretical Foundation

1 Atom-Light Interaction

Experiments in the field of quantum optics are based on the interaction between atoms, light fields and the effects arising from them. Therefore their theory will be briefly discussed in the following chapter. A more detailed discussion can be found in [8–11].

1.1 General Concepts

The state of any quantum mechanical system can be described by using the density matrix operator

$$\rho_{ij} = |i\rangle \langle j| \tag{1.1}$$

where the population of the state $|i\rangle$ is given by the diagonal element ρ_{ii} and the coherence between the states $|i\rangle$ and $|j\rangle$ by ρ_{ij}. The density operator is hermitian ($\rho = \rho^\dagger$) and for a closed system the population has to be conserved, which results in $\text{trace}(\rho) \stackrel{!}{=} 1$.
The temporal evolution is given by the von Neumann equation

$$\frac{\partial \rho(t)}{\partial t} = -\frac{i}{\hbar} \left[\hat{H}(t) \, , \hat{\rho}(t) \right] \tag{1.2}$$

with the Hamiltonian H and reduced Planck constant $\hbar$.
In the following the specific quantum mechanical system shall consists of an atom with n degenerate, non interacting energy levels that interacts with a light field $\boldsymbol{E}$. The Hamiltonian of this system consists of two parts, the Hamiltonian of the atom H_{atom} and the interaction with the light field H_{int}

$$H = H_{\text{atom}} + H_{\text{int}}. \tag{1.3}$$

In the eigenbasis of the atom H_{atom} is given by the eigenstates $|i\rangle$ and corresponding eigenvalues $\hbar\omega_i$ derived from the transition frequency ω_i:

$$H_{\text{atom}} = \sum_i \hbar\omega_i \, |i\rangle \langle i| \, . \tag{1.4}$$

The light field is assumed to be classical and furthermore any interaction with the magnetic moment of the atom is neglected due to small contribution. The interaction is therefore given by

$$H_{\text{int}} = -\boldsymbol{dE} \tag{1.5}$$

with the dipole operator $\boldsymbol{d}$ of the atom. Additionally the light field is assumed to be a plane wave propagating in z-direction

$$\boldsymbol{E}(z,t) = \frac{1}{2}\left(E_0(z,t)\, e^{i\left(\omega_{\mathrm{L},ij}t - k_{\mathrm{L},ij}z\right)} + E_0(z,t)^*\, e^{-i\left(\omega_{\mathrm{L},ij}t - k_{\mathrm{L},ij}z\right)}\right)\boldsymbol{e_z} \tag{1.6}$$

with the frequency $\omega_{\mathrm{L},ij}$, wavenumber $k_{\mathrm{L},ij} = \omega_{\mathrm{L},ij}/c$ with the speed of light c, amplitude E_0 and the unit vector $\boldsymbol{e_z}$ in propagation direction.
The von Neumann equation does not include the finite lifetime of the excited states of an atom, which is caused by different decay and dephasing effects e.g. spontaneous emission or collisions between the atoms. Those are included in the so called von Neumann equation in Lindblad form

$$\frac{\partial\rho(t)}{\partial t} = -\frac{i}{\hbar}\left[H(t)\,,\rho(t)\right] + L(\rho(t))\,. \tag{1.7}$$

The Lindblad operator [12] is defined as

$$L(\rho(t)) = L_{\mathrm{decay}}(\rho(t)) + L_{\mathrm{deph}}(\rho(t)) \tag{1.8}$$

$$= \sum_{\{i\to j\}} \Gamma_{i\to j}\left(|f\rangle\,\rho_{ii}\,\langle f| - \frac{1}{2}\left\{|i\rangle\,\langle i|\,,\rho\right\}\right) + \sum_i \gamma_{i,\mathrm{deph}}\left(|i\rangle\,\rho_{ii}\,\langle i| - \frac{1}{2}\left\{|i\rangle\,\langle i|\,,\rho\right\}\right) \tag{1.9}$$

with the decay and dephasing rates Γ and γ_{deph}, respectively.
In order to solve eq. (1.7) analytically the system is transformed to a reference frame which rotates with the frequency of the light field and subsequently fast oscillating terms are neglected. This is the so called 'Rotating Wave Approximation' (RWA) and is discussed in more detail in [8]. The diagonal transformation matrix U is given by

$$U_{ii} = \exp\left(-i\varphi_{|1\rangle\to|i\rangle}\,|i\rangle\,\langle i|\right) \tag{1.10}$$

with the accumulated phase

$$\varphi_{|1\rangle\to|i\rangle} = \sum_{\{ab||1\rangle\to|i\rangle\}} {}^{+}\!/\!_{-}\left(\omega_{\mathrm{L},ab}t - \boldsymbol{k}_{\mathrm{L},ab}\boldsymbol{x}\right) \tag{1.11}$$

$$= \sum_{\{ab||1\rangle\to|i\rangle\}} {}^{+}\!/\!_{-}\varphi_{ab} \tag{1.12}$$

where a positive sign corresponds to an absorbed photon and a negative sign to an emitted one. When transforming the density matrix the diagonal elements are not effected, $\tilde{\rho_{ii}} = \rho_{ii}$, whereas the new off diagonal elements are

$$\tilde{\rho_{ij}} = \rho_{ij}e^{i\varphi_{|i\rangle\to|j\rangle}}\,. \tag{1.13}$$

The diagonal entries of the Hamiltonian yield

$$(\tilde{H})_{ii} = \hbar\omega_i \, {}^{+}\!/_{-} \sum_{\{ab||1\rangle\to|i\rangle\}} \hbar\omega_{\mathrm{L},ab} \tag{1.14}$$

$$= \hbar \, {}^{-}\!/_{+} \sum_{\{ab||1\rangle\to|i\rangle\}} \Delta_{ab} \tag{1.15}$$

with the multiphoton detuning given by the sum over all detunings ${}^{-}\!/_{+}\Delta_{ab}$, where the sign depends on whether the photon gets absorbed or emitted. The off diagonal part of the Hamiltonian is given by

$$(\tilde{H})_{ij} = \frac{1}{2}\hbar\Omega_{ij} \left|i\right\rangle \left\langle j\right| \tag{1.16}$$

with the Rabi frequency

$$\Omega_{ij} = -\frac{d_{ij}E_{0,ij}}{\hbar} \tag{1.17}$$

and dipole transition matrix element d_{ij} from level i to j. For a Gaussian beam with a $1/e^2$ waist radius w_r and power P the electric field is given by

$$E_0 = \sqrt{\frac{4P}{c\epsilon_0\pi w_r^2}} \tag{1.18}$$

with the vacuum permittivity ϵ_0, leading to

$$\Omega_{ij} = -\frac{d_{ij}}{\hbar}\sqrt{\frac{4P}{c\epsilon_0\pi w_r^2}}. \tag{1.19}$$

The Lindblad operator is invariant under the RWA.
Using this set of equations all systems discussed in the scope of this thesis can be described.

1.2 Transition Dipole Moment

The origin of the transition dipole moment, arising from the coupling of the involved levels, will now be discussed in more detail. The derivation and notation is based on [13].
In order to calculate the Rabi frequency according to eq. (1.17) the dipole matrix element for the corresponding transition is necessary. In general for the transition between two hyperfine sublevels this is given by $d_{ij} = \langle F m_F | \, e\boldsymbol{r} \, | F' m_F' \rangle$, with the position vector $\boldsymbol{r}$ and total angular momentum quanten number of the atom F, where the prime marks the final state. It is useful to transform $\boldsymbol{r}$ into the spherical basis where the angular part

can be factored out and written as a product of Clebsch-Gordan coefficients using the Wigner-Eckart theorem

$$\langle Fm_F|\, er_q\, |F'm'_F\rangle = \langle F||e\boldsymbol{r}||F'\rangle\, (-1)^{F'-1+m_F}\sqrt{2F+1}\begin{pmatrix} F' & 1 & F \\ m'_F & q & -m_F\end{pmatrix}. \tag{1.20}$$

Here (...) denotes the Wigner-3j symbol and $\langle ...||e\boldsymbol{r}||...\rangle$ the reduced matrix element. In order to further simplify the radial part one can transform into the basis of the total angular momentum J

$$\langle F||e\boldsymbol{r}||F'\rangle = \langle J||e\boldsymbol{r}||J'\rangle\, (-1)^{F'+J+1+I}\sqrt{(2F'+1)\,(2J+1)}\begin{Bmatrix} J & J' & 1 \\ F' & F & I\end{Bmatrix} \tag{1.21}$$

with the nuclear spin I and Wigner-6j symbol $\{...\}$. Further transformation into the basis of the orbital angular momentum L yields

$$\langle J||e\boldsymbol{r}||J'\rangle = \langle L||e\boldsymbol{r}||L'\rangle\, (-1)^{J'+L+1+S}\sqrt{(2J'+1)\,(2L+1)}\begin{Bmatrix} L & L' & 1 \\ J' & J & S\end{Bmatrix} \tag{1.22}$$

with the electron spin S. The value for $\langle L||e\boldsymbol{r}||L'\rangle$ can be expressed using the radial wavefunctions $R_{nl}(r)$ and theoretically calculated from the overlap integral of the two states.
When assuming near resonance excitation and non degenerate hyperfine levels the effective dipole moment for one F transition is given by

$$|\langle F||e\boldsymbol{r}||F'\rangle|^2 = S_{FF'}\,|\langle J||e\boldsymbol{r}||J'\rangle|^2 \tag{1.23}$$

with the relative hyperfine transition strength factors

$$S_{FF'} = (2F'+1)\,(2J+1)\begin{Bmatrix} J & J' & 1 \\ F' & F & I\end{Bmatrix}^2. \tag{1.24}$$

For a far detuned excitation all hyperfine states are addressed and therefore the sum over all transition strengths has to be considered and because

$$\sum_{F'} S_{FF'} = 1 \tag{1.25}$$

this leaves

$$|\langle F||e\boldsymbol{r}||F'\rangle|^2 = |\langle J||e\boldsymbol{r}||J'\rangle|^2. \tag{1.26}$$

1.3 Two-Level Atom

In order to illustrate the basic principles of atom-light interactions an atomic system with only two non-degenerate energy levels is considered in the following section. The resulting level scheme for this is shown schematically in fig. 1.1. Here the angular transition frequency between the ground state $|1\rangle$ and excited state $|2\rangle$ is given by the difference of the corresponding eigenenergies $\omega_0 = \omega_2 - \omega_1$, the excited state decays to the ground state with a rate Γ, while the levels are coupled by a light field with the energy $\hbar\omega_\mathrm{L}$ and a frequency detuning in relation to the transition frequency of $\Delta = \omega_\mathrm{L} - \omega_0$. With $|1\rangle = \binom{1}{0}$ and $|2\rangle = \binom{0}{1}$ the Hamilton and Lindblad operator from eqs. (1.3) and (1.9) are given by

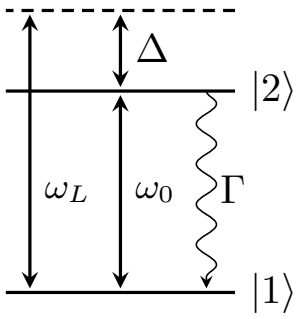

Figure 1.1: Level scheme of a two-level system. The variables are defined in the text.

$$H = \hbar \begin{pmatrix} 0 & \frac{1}{2}\Omega \\ \frac{1}{2}\Omega^* & \Delta \end{pmatrix} \tag{1.27}$$

and

$$L_D = \Gamma \begin{pmatrix} \tilde{\rho}_{22} & -\frac{1}{2}\tilde{\rho}_{12} \\ -\frac{1}{2}\tilde{\rho}_{21} & -\tilde{\rho}_{22} \end{pmatrix}. \tag{1.28}$$

With those, the von Neumann equation (1.7) can be set up. After simplifying the resulting coupled differential equations are

$$\frac{\partial}{\partial t}\tilde{\rho}_{11} = \Gamma\tilde{\rho}_{22} - \mathrm{Im}\left(\tilde{\rho}_{12}\Omega^*\right) \tag{1.29a}$$

$$\frac{\partial}{\partial t}\tilde{\rho}_{12} = \left(-\frac{\Gamma}{2} - i\Delta\right)\tilde{\rho}_{12} - i\frac{\Omega}{2}\left(\tilde{\rho}_{22} - \tilde{\rho}_{11}\right) \tag{1.29b}$$

$$\frac{\partial}{\partial t}\tilde{\rho}_{21} = \left(-\frac{\Gamma}{2} - i\Delta\right)\tilde{\rho}_{12} + i\frac{\Omega}{2}\left(\tilde{\rho}_{22} - \tilde{\rho}_{11}\right) \tag{1.29c}$$

$$\frac{\partial}{\partial t}\tilde{\rho}_{22} = -\Gamma\tilde{\rho}_{22} + \mathrm{Im}\left(\tilde{\rho}_{12}\Omega^*\right) \tag{1.29d}$$

which are also known as the Optical Bloch Equations.
To further understand the dynamics of the system, a solution for an on resonance excitation with the initial condition, that initially all atoms are in the ground state

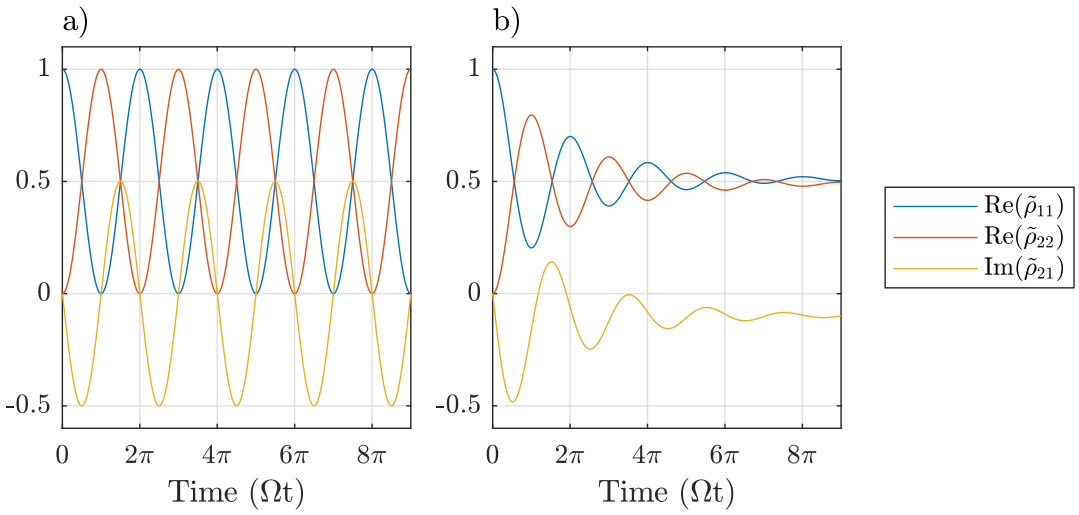

Figure 1.2: Time evolution of a two-level system with the initial condition $\tilde{\rho}_{11}(t=0) = 1$, $\Delta = 0$ and a) $\Gamma = 0$ and b) $\Gamma = 0.2 \cdot \Omega$

$\tilde{\rho}_{11}(t = 0) = 1$ can be seen in fig. 1.2. The special case where the excited state has an infinite lifetime, $\Gamma = 0$, can be seen in fig. 1.2 a). Here, the population of atoms simply oscillates between the two energy levels with the angular frequency equaling the Rabi frequency. This coherent population transfer is called Rabi oscillation. When the finite lifetime of the excited state is included, $\Gamma \neq 0$, the Rabi oscillations are damped, which can be seen in fig. 1.2 b). For long timescales $t \gg \frac{1}{\Gamma}$ a steady state regime is reached. This can be derived from eq. (1.29) with $\frac{\partial}{\partial t}\tilde{\rho} = 0$ and its solution is given by:

$$\tilde{\rho}_{11} = \frac{|\Omega|^2 + 4\Delta^2 + \Gamma^2}{2|\Omega|^2 + 4\Delta^2 + \Gamma^2} \tag{1.30a}$$

$$\tilde{\rho}_{12} = \frac{\Omega(2\Delta + i\Gamma)}{2|\Omega|^2 + 4\Delta^2 + \Gamma^2} \tag{1.30b}$$

$$\tilde{\rho}_{21} = \frac{\Omega^*(2\Delta - i\Gamma)}{2|\Omega|^2 + 4\Delta^2 + \Gamma^2} \tag{1.30c}$$

$$\tilde{\rho}_{22} = \frac{|\Omega|^2}{2|\Omega|^2 + 4\Delta^2 + \Gamma^2}. \tag{1.30d}$$

1.3.1 Optical Response

In the experiments presented later the measured quantity is the light intensity after interacting with a number of atoms. So in order to compare theoretical calculations and experimentally determined values, the response to the electromagnetic fields of the

atoms is required. This can be done via the electric susceptibility χ which is defined by the polarizability P of the medium

$$\boldsymbol{P} = \epsilon_0 \chi \boldsymbol{E} \tag{1.31}$$

$$= \frac{1}{2}\epsilon_0 \chi \boldsymbol{E_0} e^{-i\omega_\mathrm{L} t} + \text{c.c.} \ . \tag{1.32}$$

Analogously, the polarizability can also be calculated for an atomic ensamble with the density n

$$\boldsymbol{P} = n \langle \boldsymbol{d} \rangle \tag{1.33}$$

$$= n\mathrm{Trace}\left(\rho \boldsymbol{d}\right) \tag{1.34}$$

$$= n\left(\boldsymbol{d_{12}}\tilde{\rho}_{21} e^{-i\omega_\mathrm{L} t} + \boldsymbol{d_{21}}\tilde{\rho}_{12} e^{i\omega_\mathrm{L} t}\right). \tag{1.35}$$

By comparing this equation to eq. (1.32) an expression for the susceptibility can be derived:

$$\chi = -\frac{2n\left|d_{12}\right|^2}{\epsilon_0 \hbar \Omega_{12}} \tilde{\rho}_{21}. \tag{1.36}$$

The imaginary part of the susceptibility is proportional to the absorption coefficient α

$$\alpha = k_\mathrm{L} \mathrm{Im}\left(\chi\right). \tag{1.37}$$

Using the Beer-Lambert Law the corresponding intensity I after traveling through the medium for the distance l can be calculated

$$I = I_0 e^{-\alpha l}. \tag{1.38}$$

1.4 Three-Level Atom

Exciting an atom to a specific state can often not be achieved via a direct transition from the ground state for a number of reasons, e.g. laser availability or dipole selection rules. Therefore an intermediate state is necessary and the previously discussed two-level system has to be expanded to at least a three-level system. To deepen the understanding of multi level atoms, the dynamics of a three level system will be derived in this section. The level scheme can be seen in fig. 1.3, including the used notations for the transitions and decays. Equivalently to section 1.3 the Hamiltonian and Lindblad operator can be set up using the equations derived in section 1.1:

$$H = \begin{pmatrix} 0 & \frac{1}{2}\Omega_{12} & 0 \\ \frac{1}{2}\Omega_{12} & -\Delta_{12} & \frac{1}{2}\Omega_{23} \\ 0 & \frac{1}{2}\Omega_{23} & -\left(\Delta_{12} + \Delta_{23}\right) \end{pmatrix} \tag{1.39}$$

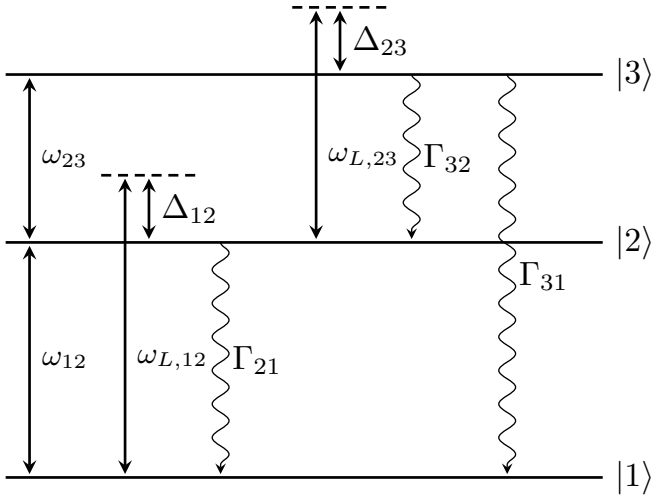

Figure 1.3: Scheme of a three level system. The variables are defined in the text.

$$L_D = \begin{pmatrix} \Gamma_{21}\tilde{\rho}_{22} + \Gamma_{31}\tilde{\rho}_{33} & -\frac{1}{2}\Gamma_{21}\tilde{\rho}_{12} & -\frac{1}{2}\left(\Gamma_{31}+\Gamma_{32}\right)\tilde{\rho}_{13} \\ -\frac{1}{2}\Gamma_{21}\tilde{\rho}_{21} & -\Gamma_{21}\tilde{\rho}_{22} + \Gamma_{32}\tilde{\rho}_{33} & -\frac{1}{2}\left(\Gamma_{21}+\Gamma_{31}+\Gamma_{32}\right)\tilde{\rho}_{23} \\ -\frac{1}{2}\left(\Gamma_{31}+\Gamma_{32}\right)\tilde{\rho}_{31} & -\frac{1}{2}\left(\Gamma_{21}+\Gamma_{32}+\Gamma_{31}\right)\tilde{\rho}_{32} & -\left(\Gamma_{31}+\Gamma_{32}\right)\tilde{\rho}_{33} \end{pmatrix}. \tag{1.40}$$

With them the optical Bloch equations can be set up and solved. In contrast to the two level system there are additional distinctive effects, which can be observed in a three level system.

1.4.1 Electromagnetically Induced Transparency

One of those effects is electromagnetically induced transparency (EIT). Here, an atomic transition coupled by a weak light field (probe field) becomes transparent on resonance when a second strong light field (coupling field), which couples one of the involved states to a third one, is applied. This can be seen in fig. 1.4. Without the coupling light field ($\Omega_{23} = 0$) the probe field gets absorbed with a maximum on resonance, but for an increasing coupling field a transmission window around the resonance appears and becomes broader for higher coupling frequencies and two separate absorption peaks arise. This effect is called Autler Townes splitting and emerges for higher coupling frequencies from the EIT regime, whereby the two areas can not be clearly separated from each other [14].

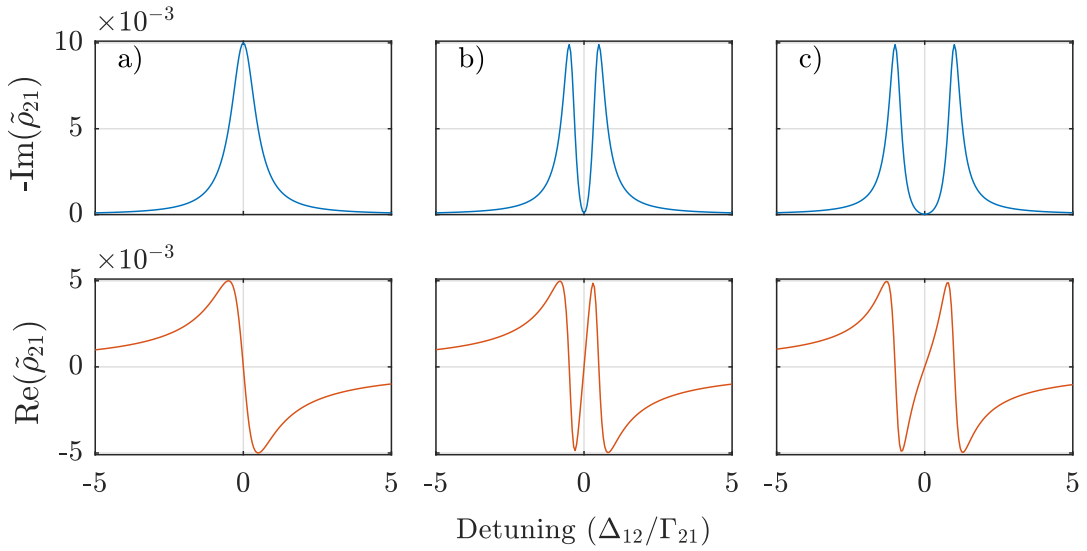

Figure 1.4: Imaginary (top) and real (bottom) part of $\tilde{\rho}_{21}$ with $\Omega_{12} \ll \Gamma_{21}$ and $\Gamma_{32} \gg \Gamma_{21}$ for increasing coupling frequencies a) $\Omega_{23}/\Gamma_{21} = 0$, b) $\Omega_{23}/\Gamma_{21} = 1$ and c) $\Omega_{23}/\Gamma_{21} = 2$.

1.4.2 Autler-Townes Splitting

In order to explain the splitting of the absorption signal for high coupling frequencies one has to take a closer look at the three level Hamiltonian in eq. (1.39). If we assume two-photon resonance ($\Delta_{12} + \Delta_{23} = 0$) $|1\rangle$, $|2\rangle$ and $|3\rangle$ are no longer eigenstates of the system, but by diagonalizing, new eigenstates, the so called 'dressed states' [10]

$$|0\rangle = \cos\theta\,|1\rangle - \sin\theta\,|3\rangle \tag{1.41a}$$
$$|-\rangle = \sin\theta\cos\phi\,|1\rangle - \sin\phi\,|2\rangle + \cos\theta\cos\phi\,|3\rangle \tag{1.41b}$$
$$|+\rangle = \sin\theta\sin\phi\,|1\rangle + \cos\phi\,|2\rangle + \cos\theta\sin\phi\,|3\rangle \tag{1.41c}$$

can be derived with the mixing angles

$$\tan\theta = \frac{\Omega_{12}}{\Omega_{23}} \tag{1.42a}$$
$$\tan(2\phi) = \frac{\sqrt{\Omega_{12}^2 + \Omega_{23}^2}}{\Delta_{12}} = \frac{\Omega_{2\mathrm{ph}}}{\Delta_{12}} \tag{1.42b}$$

and the effective two photon Rabi frequency $\Omega_{2\mathrm{ph}} = \sqrt{\Omega_{12}^2 + \Omega_{23}^2}$. For a weak probe frequency thus $|0\rangle$ corresponds to the previous ground state $|1\rangle$ and the other two states $|\pm\rangle$ are the superposition of the previous intermediate and excited state with

$$|\pm\rangle = \frac{1}{\sqrt{2}}\left(|2\rangle \pm |3\rangle\right). \tag{1.43}$$

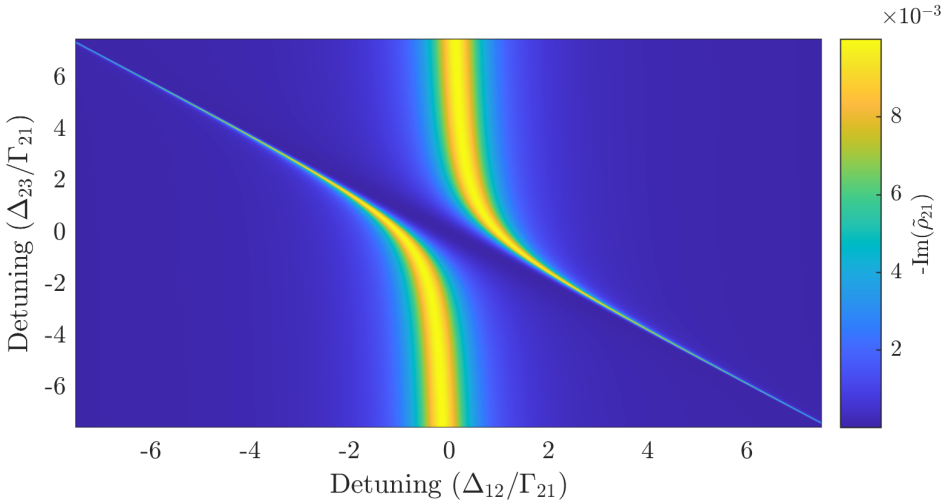

Figure 1.5: $\mathrm{Im}(\tilde{\rho}_{21})$ as a function of the probe and coupling detuning with $\Omega_{12}/\Gamma_{21} = \frac{1}{100}$, $\Omega_{23}/\Gamma_{21} = 2$ and $\Gamma_{21} = 100 \cdot \Gamma_{32}$

It can be easily seen that for $|0\rangle$ the eigenenergy remains zero, whereas $|+\rangle$ and $|-\rangle$ are shifted by

$$E_\pm = \frac{1}{2}\left(\Delta_{12} \pm \sqrt{\Delta_{12}^2 + \Omega_{12}^2 + \Omega_{23}^2}\right) = \frac{1}{2}\left(\Delta_{12} \pm \sqrt{\Delta_{12}^2 + \Omega_{2\mathrm{ph}}^2}\right) \tag{1.44}$$

respectively. Subsequently the observed splitting is $\Omega_{2\mathrm{ph}}$. In fig. 1.5 the absorption signal for different probe and coupling detunings is shown. Here the avoided crossing at zero two-photon detuning ($\Delta_{12} = -\Delta_{23}$) can be clearly observed, but for high detunings the dressed states are slowly approaching the initial eigenstates again.

1.5 Broadening Effects

The natural linewidth of an atomic transition has a Lorentzian lineshape whose width is given by the lifetime of the exited state, but there are additional effects, that lead to a further broadening.

1.5.1 Doppler Broadening

One property that has not been considered so far is the movement of the atoms caused by the temperature of the ensemble. This movement results in an additional and for each atom individual frequency shift $\Delta_\mathrm{D} = \boldsymbol{kv}$ with the velocity $\boldsymbol{v}$ of the atom and the wavevector $\boldsymbol{k}$ of the light field. This means, that slightly off resonant light appears to be on resonance for atoms moving with a specific velocity that compensates for the initial

offset. To take this into account the Doppler detuning has to be added to the laser detunings in the Hamiltonian in eq. (1.3) with

$$\Delta_{ij,\mathrm{D}} = \Delta_{ij} - \boldsymbol{k_L v}. \tag{1.45}$$

In a thermal vapor the velocity classes are Maxwell-Boltzmann distributed in all spatial directions. Due to the scalar product in eq. (1.45) only atoms moving parallel to the light field need to be considered, so an 1-dimensional Gaussian distribution is sufficient:

$$f(v,T) = \sqrt{\frac{m}{2\pi k_B T}} \exp\left(-\frac{mv^2}{2k_B T}\right) \tag{1.46}$$

with the Boltzmann constant k_B, atom mass m and Temperature T. The resulting lineshape $h(\Delta_{ij})$ of the transition is the convolution of the natural Lorentz $g(\Delta_{ij} - \boldsymbol{k_L v})$ and the Doppler broadened Gaussian lineshape which results in a Voigt profile

$$h(\Delta_{ij},T) = \int_{-\infty}^{\infty} f(v,T)\, g(\Delta_{ij} - \boldsymbol{k_L v})\, dv. \tag{1.47}$$

For experiments with atoms at, or above room temperature, the Doppler broadening is usually orders of magnitude larger than the natural linewidth so the lineshape can be approximated to be only Gaussian.

1.5.2 Transit Time Broadening

The finite size of the laser beam used for the excitation of the atoms is also causing an additional broadening, the so called transit time broadening, as atoms can simply move out of the excitation volume given by the laser geometry. In approximation one can assume that for every atom flying out of the beam another atom is flying into it, which is however in the ground state. In the formalism of the Lindblad operator, this is given by a decay rate coupling every level directly to the ground state. The timescale of this effect can be estimated by taking the average velocity $\overline{v}$ of the Maxwell Boltzmann distribution

$$\overline{v}(T) = \sqrt{\frac{\pi k_B T}{2m}} \tag{1.48}$$

and calculating the time they need for the average path $\overline{d}$ orthogonal to a Gaussian beam with $1/e^2$ beam radius w_r

$$\overline{d} = \frac{\pi}{4}\sqrt{2\ln(2)}w_r. \tag{1.49}$$

This results in

$$\Gamma_{tt} = \frac{\overline{v}}{\overline{d}} = \frac{2}{\sqrt{\pi \ln(2)}}\sqrt{\frac{k_B T}{m}}\frac{1}{w_r}. \tag{1.50}$$

Especially for strongly focused laser beams with a small waist, or at really high temperatures this decay becomes the dominating factor.

2 Rydberg Atoms

2.1 General Properties

Rydberg atoms are atoms with at least one valence electron excited to a state with a high principle quantum number (typically $n > 15$), the so called Rydberg states [4]. In the following section the case with exactly one electron in the Rydberg state will be discussed. Due to the large distance between this electron and the nucleus, shielded by the core electrons, the atom can be considered hydrogen-like and subsequently be described via the Bohr model with the energy levels

$$E_{n^*} = -\frac{1}{(4\pi\epsilon_0)^2}\frac{e^4 m_e}{2\,(n^*)^2\,\hbar^2} \tag{2.1}$$

with the elementary charge e, electron mass m_e, vacuum permittivity ϵ_0 and the effective principle quantum number $n^* = n - \delta_{n,l,j}$. The quantum defect $\delta_{n,l,j}$ takes into account, that the ionic core is not, as assumed in the Bohr model, point like but has a structure and can be calculated from the Rydberg-Ritz formula, a series expansion in n

$$\delta_{n,l,j} = \delta_0 + \frac{\delta_2}{(n-\delta_0)^2} + \frac{\delta_4}{(n-\delta_0)^4} + \frac{\delta_6}{(n-\delta_0)^6} + \cdots \tag{2.2}$$

wherein the coefficients δ_i must be determined experimentally for each state and atom. E.g. for rubidium S-states those values can be found in [15]. The electron in the Rydberg state is only weakly bound to the nucleus due to its large distance. This leads to some interesting properties of the atom like a long lifetime or a high sensitivity to external fields. More properties of Rydberg atoms and the corresponding scaling laws can be found in table 2.1.

Table 2.1: Scaling laws for properties of Rydberg atoms [4]

property	scaling
orbital radius	$(n^*)^{-3}$
binding energy	$(n^*)^{-2}$
lifetime	$(n^*)^{3}$
polarizability	$(n^*)^{7}$

2.2 Rydberg-Rydberg Interactions

Due to their high polarizability Rydberg atoms are not only sensitive towards externally applied electric and magnetic fields, but also towards other Rydberg atoms. This leads, among other effects, to the so-called Rydberg blockade: A Rydberg atom induces an electric field which shifts the eigenenergies of the eigenstates from all neighboring atoms. If the bandwidth of the optical excitation to the Rydberg state is smaller than this energy shift the neighboring atoms can not be excited to the Rydberg state, which means depending on the interaction strength and excitation bandwidth a so called blockade volume can be calculated in which only one atom is excited to the Rydberg state. This Rydberg-Rydberg interaction is van der Waals like and therefore scales proportional to $\frac{1}{r^6}$ with the distance r between the atoms [16].

3 Rubidium

Rubidium is part of the alkali metal group and accordingly has only one valence electron. The two naturally abundant isotopes are the stable ^{85}Rb (72.17 %) [13] and the semi stable ^{87}Rb (27.83 %) with a nuclear lifetime of $4.88 \cdot 10^{10}$ years [17]. Both isotopes have a melting point at around 39.3 °C [13, 17]. In a confined volume V with temperature T the atomic density $N = N_0/V$ can be calculated by using the ideal gas law $P_V V = k_B N_0 T$ wherein the vapor pressure P_V in torr is given by

$$\log_{10} P_V = 2.881 + 4.312 - \frac{4040}{T} \tag{3.1}$$

for liquid rubidium [13] with the temperature T in kelvin. The resulting curve can be seen in fig. 3.1.
The level scheme for the two isotopes including the hyperfine structure of the, in the scope of this thesis important, 5S and 6P states can be found in appendix A.
For all experiments performed in this theses, cells filled with natural rubidium were used so accordingly ^{85}Rb and ^{87}Rb occur in the previously described ratio.

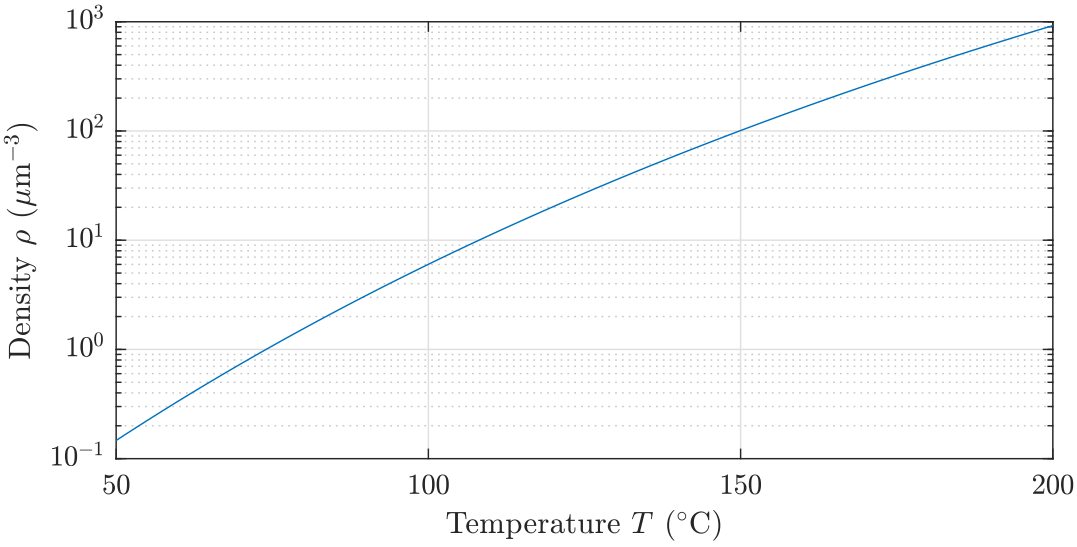

Figure 3.1: Atomic density of rubidium calculated from the vapor pressure as a function of the temperature

Part II

Laser Setup

4 Frequency Stabilization

A crucial part of every experiment in the field of atomic physics is the reliable control of the frequency of the lasers. In principle to do so an absolute frequency reference and a way to stabilize the laser at the desired frequency are needed. To determine the absolute frequency some form of atomic reference is required, since the frequency can not be resolved otherwise. If this is not possible for the desired wavelength one can use a reference laser with known frequency (specified with an atomic transition) and then measure the relative frequency difference between the two lasers with an interferometer. This is the working principle of commercially available wavelength meters. The accuracy of such devices can vary from tenths of a nanometer to far below 1 pm. For the experiments presented in this thesis the coarse adjustment of the laser frequencies were done with a wavelength meter and the fine adjustment with corresponding rubidium transitions.

4.1 Optical Resonator

A practical way to determine the absolute frequency change of a laser is an optical resonator e.g. a Fabry–Pérot interferometer consisting of one planar and one concave mirror. In the following section this specific type of optical resonator is referred to as cavity. The two mirrors of the cavity have a spacing d. As the light gets confined in the cavity and reflects multiple times before exiting through one of the mirrors a standing wave is formed inside the cavity with a certain resonance frequency, producing the characteristic transmission signal which can be seen in fig. 4.1. The main features of a cavity are the free spectral range

$$\delta\nu = \frac{c}{2d} \tag{4.1}$$

which defines the frequency distance between two adjacent transmission peaks and the finesse

$$\mathcal{F} = \frac{\delta\nu}{\Delta\nu} \tag{4.2}$$

defined as the free spectral range divided by the full with at half-maximum bandwidth of the transmission peak $\Delta\nu$. The finesse is a relative measure on how sharp the frequency resonances are.
By observing the position of the transmission peaks, a change in the frequency of the laser can be detected if the spacing is fixed. In order to stabilize the frequency two

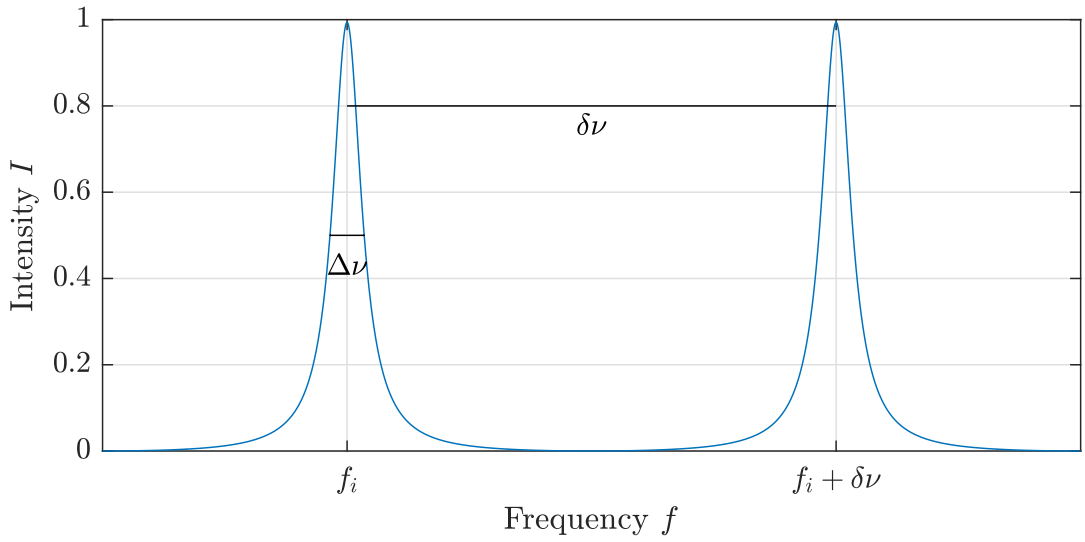

Figure 4.1: Transmitted intensity of the cavity with the linewidth $\delta\nu$ and free spectral range $\Delta\nu$.

things are needed; an error signal which gives the difference between the current and the desired frequency (from now on referred to as set point) and a feedback loop to counteract the change.

4.2 Pound-Drever-Hall Technique

One possible error signal would be the transmission signal of the cavity and define the set point to the steep side fringe. The main difficulty with this technique is, that there is no way to distinguish between an intensity change and a frequency change. To eliminate this problem the so called Pound-Drever-Hall (PDH) technique [18] is used. The interesting part here is the phase of the signal which on resonance not only has a zero crossing but also changes sign. Unfortunately photo detectors are not able to directly resolve the phase of an optical signal. A method to determine the phase is through interference. An elegant way to do this is by phase modulating the laser frequency (usually done with an electro-optical modulator (EOM)), creating side bands in the frequency domain. The interference between those and the main frequency is then detected on the photo diode and by demodulating the signal with the modulation frequency the Pound-Drever-Hall error signal can be obtained as shown in fig. 4.2. But as the sidebands are not transmitted through the cavity the transmitted light is not suited as an optical signal but the reflected light. This is a combination of the light which gets directly reflected at the first mirror and the part entering and leaving the cavity from the same mirror after multiple round trips. If the laser frequency matches the resonance frequency of the cavity both parts cancel out each other and the reflection signal goes to zero. For simplicity, the reflection

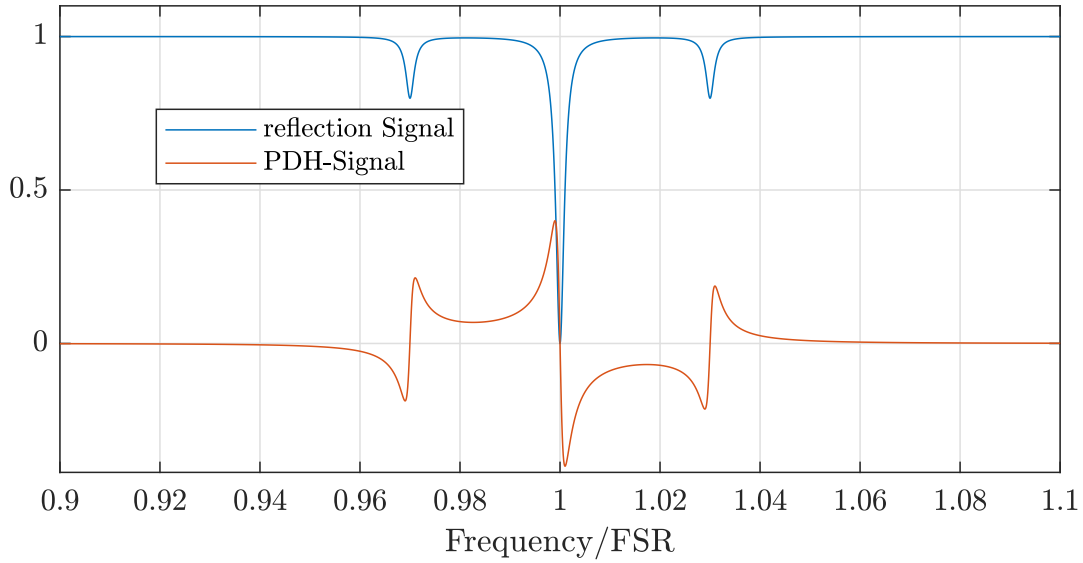

Figure 4.2: Reflection signal of the cavity and corresponding Pound-Drever-Hall signal

signal can be thought of as the inverted transmission signal with respect to the phase. A detailed theoretical description of the PDH-technique can be found in [19].

4.3 PID Controller

For the feedback loop a commonly used technique is the proportional-integral-derivative (PID) controller. As the name already suggests it consist of three parts. The proportional component only takes the difference between the current signal and the set point and gives an output proportional to that. This leads to the fact, that with a proportional controller itself in theory the set point can never be reached, in practical use one can increase the proportional response to reach the set point but that will lead to the system oscillating. To prevent this the integrational part is added which is proportional to the sum of the error signal over time. A controller consisting of those two components (PI-controller) is for some applications already sufficient enough. The only remaining problem is the risk of overshooting which happens especially with fast changing signals. In order to also regulate those the derivative part is added. It decreases the output if the signal is changing too fast and will thereby not only reduce overshooting but also increase the overall speed of the controller.
To get the best possible performance of a PID controller all parts have to be set in the right proportion to each other and adjusted to the application.

4.4 Transfer Lock

By combining the PDH-technique and a PID controller in theory, a stable and reliable laser lock can be achieved. In practice, however, there are some problems which also have to be considered. For example temperature and air pressure can not only cause the properties of optical components to change slightly, but also influence the refractive index of air. Both lead to a change of the optical path d in the cavity and thereby change the main properties. In order to reduce those effects an ultra-low-expansion (ULE) cavity can be used which is an active temperature stabilized Fabry–Pérot interferometer, where the space between the two mirrors is filled with a glass block made from ultra low expansion glass. For the final pulsed four-wave-mixing experiment however a total of four lasers have to be frequency locked, where two have a blue and two an infrared wavelength. This makes it first of all more complicated to find an ULE cavity, that works for all of those wavelengths and as especially the two blue lasers are very close to each other in wavelength it would be hard to overlap and separate them in the same ULE cavity. Also the laser locking setup should be constructed in a way that it is possible to add lasers with other wavelengths at a later point in time. Therefore the most suitable system is using transfer cavities. The working principle is based on one reference laser and multiple transfer lasers. The reference laser is locked on the ULE cavity and its frequency can be chosen freely. The locked laser is then sent on an additional cavity consisting of an planar mirror mounted on an piezo to remotely adjust the distance to the second concave mirror. As scanning the length of the cavity has the same effect as scanning the laser frequency, the reference laser and piezo voltage of the transfer cavity can be used to actively stabilize the length of the cavity against unwanted drifts. Lastly another laser (referred to as transfer laser) is coupled into the same transfer cavity and frequency stabilized onto this one. In both cases EOMs are used to modulate the frequency sidebands. Later in the experiments it should be possible to choose the locking point freely, e.g. to be exactly on resonance with an atomic transition, therefore a second modulation frequency is applied to the EOM in the order of $50 - 500\,\mathrm{MHz}$. In contrast to the modulation for the PDH-signal here the amplitude is optimized for maximum signal in the first order, which will be used as locking signal. By changing the modulation frequency the position of the first order relative to the non modulated signal can be shifted and accordingly also the locking position. If the modulation range of the EOM is larger than half the free spectral range of the cavity, it is possible to lock the laser to every wavelength.
The schematic setup of a transfer cavity can be seen in fig. 4.3. Both lasers first pass through a polarizing beam splitting cube in transmission, a quarter waveplate and a lens (l_1 and l_2 respectively) which is individually calculate for optimized mode matching inside the cavity [20], before being overlapped by a dichroic mirror and coupled into the cavity. The transmitted signals get separated again using a dichroic mirror. The reflection signal, which is needed for the PDH-signal, first travels back the same way as the incoming beam until the polarizing beam splitting cube. Since it passed the

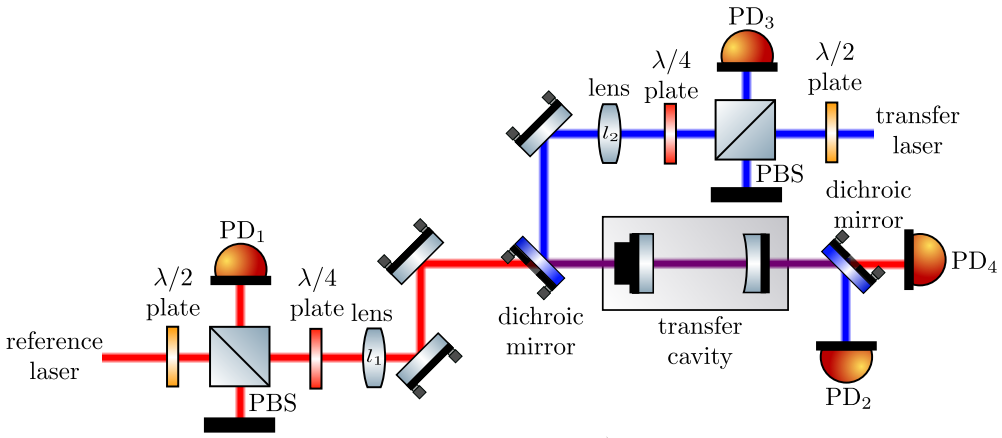

Figure 4.3: Schematic set up of the laser locking technique using a transfer cavity, reference and transfer laser.

quarter waveplate a total of two times now the polarization of the reflected beam has been rotated by 90 ° and gets reflected at the cube and can be observed on photodiodes PD_1 and PD_3 respectively.
The advantage of this system is not only that it can be extended by an arbitrary number of additional transfer lasers but it is also more cost-efficient than having multiple ULE cavities. A more detailed description of the set up and measurements on the locking performance can be found in [21].

5 Laser System

5.1 Ground State Transition

As the ground state excitation for all experiments the $5S_{1/2} \rightarrow 6P_{1/2}$ transition was used. Important properties of this transition can be calculated using [23]. For rubidium 85 they can be found in table 5.1. The corresponding spectrum can be seen in fig. 5.1 with the

Table 5.1: Optical properties for the $5S_{1/2} \rightarrow 6P_{1/2}$ transition in rubidium 85 calculated using [23].

transition wavelength	λ	421.673 nm
reduced dipole moment	$\langle J \Vert e\boldsymbol{r} \Vert J' \rangle$	$0.235\, a_0 e$
decay rate	Γ	$1.498 \cdot 10^6\, \mathrm{s}^{-1}$
lifetime	$\tau_{6P_{1/2}}$	129.3 ns

absolute values taken from [22]. This is always used as an absolute frequency reference to stabilize the laser frequency resonant to a specific hyperfine transition. Therefore, the corresponding reduced dipole moment has to be considered as derived in section 1.2. The required transition strength factors are shown in table 5.2. The used laser system

Table 5.2: Relative hyperfine transition strength factors $S_{FF'}$ for the $5S_{1/2} \rightarrow 6P_{1/2}$ transition calculated with eq. (1.24).

^{85}Rb	S_{22}	2/9	S_{32}	5/9
	S_{23}	7/9	S_{33}	4/9
^{87}Rb	S_{11}	1/6	S_{21}	1/2
	S_{12}	5/6	S_{22}	1/2

to excite the ground state transition is a TA-SHG Pro from Toptica with a fundamental design wavelength of 840.6 nm resulting in the frequency doubled output of 420.3 nm with a maximum power of roughly 70 mW. A side output of the fundamental laser was used to stabilize the laser frequency.

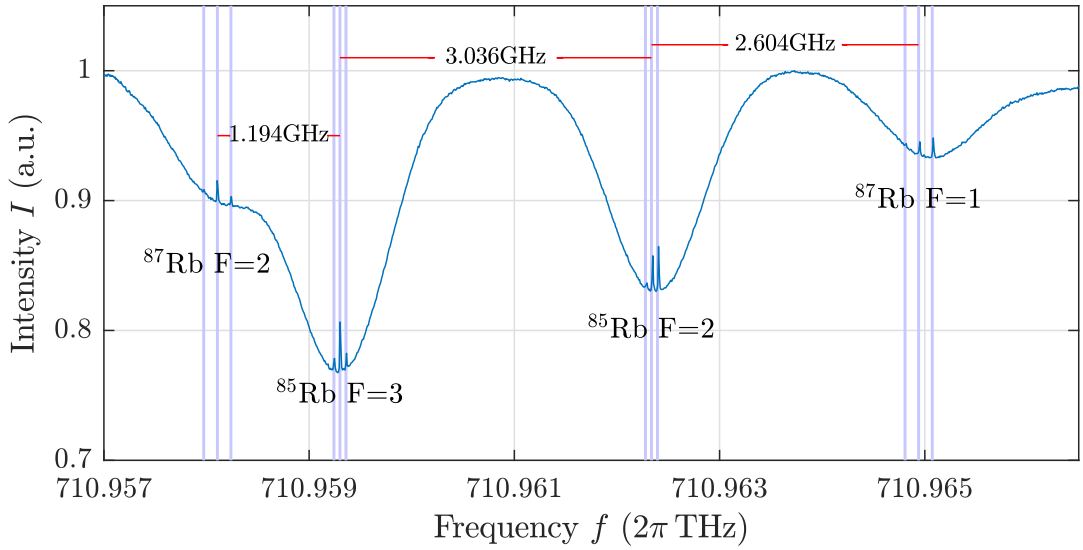

Figure 5.1: Saturation spectrum for the $5S_{1/2} \rightarrow 6P_{1/2}$ transition for natural rubidium. Values taken from [22].

5.2 Rydberg Transition

In the scope of this thesis two different Rydberg states were used, namely the $40S_{1/2}$ and $32S_{1/2}$ were excited via a two photon transition with the intermediate state $6P_{1/2}$. The relevant optical properties are shown in table 5.3.

Both transitions were investigated with the same Toptica DL pro diode laser with

Table 5.3: Optical properties for the Rydberg transition in rubidium 85 calculated using [23].

		$6P_{1/2} \rightarrow 32S_{1/2}$	$6P_{1/2} \rightarrow 40S_{1/2}$
transition wavelength	λ	1015.84 nm	1010.61 nm
reduced dipole moment	$\langle J\|\|e\boldsymbol{r}\|\|J'\rangle$	$0.033\, a_0 e$	$0.023\, a_0 e$
decay rate	Γ	$2.11 \cdot 10^3\, \mathrm{s}^{-1}$	$1.01 \cdot 10^3\, \mathrm{s}^{-1}$
lifetime	τ	30.1 μs	62.7 μs

a maximum output power of around 100 mW. When comparing the properties of the ground and Rydberg transition there are a few things to note. First of all the reduced dipole matrix element is roughly a factor 10 smaller which means in order to achieve the same Rabi frequency for identical beam parameters a 100 times higher laser power is needed. E.g. in order to achieve a Rabi frequency of around $1 \cdot 2\pi$ GHz, with a beam waist of around 40 μm the infrared laser needs a peak power of roughly 100 W. This is impossible to achieve with currently commercially available continuous wave lasers and as the four wave mixing experiment will be done with pulsed lasers anyway a custom

build pulsed amplifier will be used.

5.2.1 Pulsed Fiber Amplifier

Apart from the high peak power additional requirements for the amplifier given by the plans for the pulsed four wave mixing experiment are:

- Working range between 1008-1024 nm
- Pulse duration between 0.5-10 ns
- Pulse duration jitter < 100 ps
- Repetition rate from 50 Hz to 1 MHz

As those requirements can not be fulfilled by commercially available amplifiers, one was custom build by the Fraunhofer Institute for Applied Optics and Precision Engineering IOF in Jena [7], based on a solid state amplifier using Ytterbium doped glass fibers. The previous described diode laser is used as master oscillator, which in the first stage passes through an electro-optical intensity modulator (EOIM) to create 1 ns pulses with a repetition rate of 3 MHz. These subsequently get preamplified before passing an acousto optical modulator (AOM) where the repetition rate can be further reduced by factor 3-30. A smaller repetition rate leads to a higher amplification factor in the following amplifier, as more time passes between two pulses, leading to a higher inversion population in the gain medium of the amplifier. Before the main amplifier the pulses pass once again a preamplifier. With a second AOM the repetition rate can once again be reduced without affecting the peak power. The pulselength can be adjusted through the EOIM from roughly 1 ns to 10 ns. When changing the pulselength the repetition rate has to be adapted accordingly to guarantee a high enough inversion in the amplifier for consistent amplification over the whole duration of the pulse. Figure 5.2 shows the pulse shape for a 10 ns pulse. Here it can be seen that the amplifier is approaching its operation limit and the amplification starts to decrease over the pulse duration. But as the decrease is in the order of 20 % the pulse can still be assumed to be rectangular in a first approximation. It is also to note, that the slow decrease at the end of the pulse is due to the properties of the used photodiode as this was not observed in [7] and can therefore be neglected.

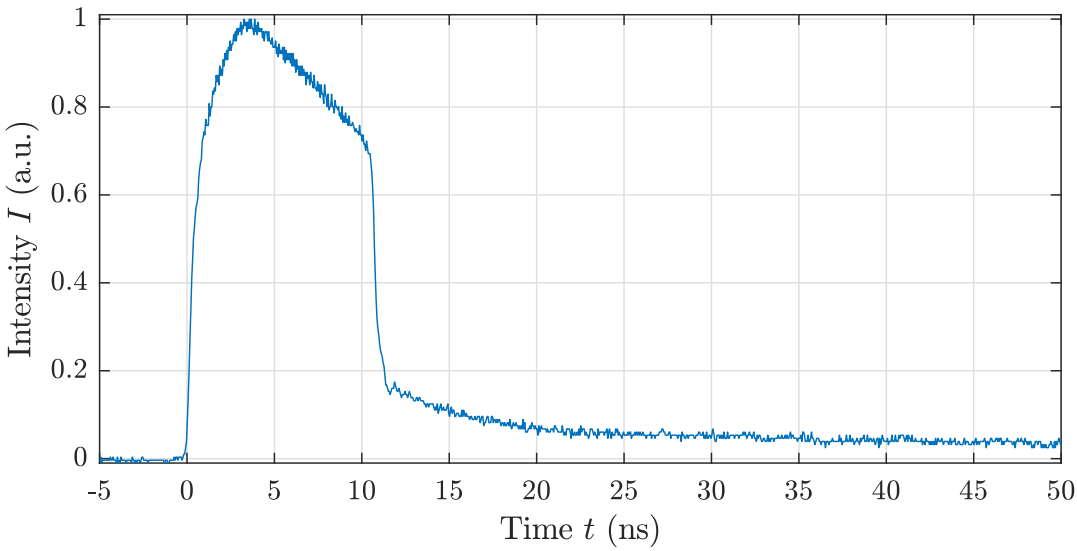

Figure 5.2: Measured single shot temporal pulse shape for a pulselength of 10 ns and with a repetition rate of 100 kHz.

Part III

Thermal Steady State Rydberg Spectroscopy

Introduction

The first important step towards pulsed four wave mixing is exciting the Rydberg atoms in the two photon scheme with continuous wave lasers. This is not only needed as the mandatory absolute frequency reference for the Rydberg transition, but also to examine the occurring effects like Autler Townes Splitting and EIT.
In this part the experimental setup is described, before the underlying principle for simulating steady state experiments is presented. Subsequently, the experimental results are shown and compared to simulations.

Figure 5.3 shows the used excitation scheme. The interesting part of this is, that the probe wavelength with 422 nm is shorter than the coupling wavelength 1011 nm. At room temperature this can lead to unique features due to the response of different velocity classes and has been studied before using a similar levelscheme in cesium [24].

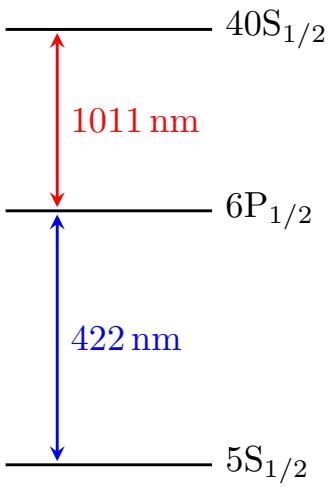

Figure 5.3: Excitation scheme used for the continuous wave Rydberg spectroscopy.

6 Experimental Setup

In fig. 6.1 the experimental setup can be seen. The blue probe laser, which corresponds to the ground state transition is divided into two arms such that their the power ratio can be manually adjust through a $\lambda/2$ waveplate and polarizing beamsplitting cube combination. Inside the 20 cm long rubidium cell both beams are overlapped again in counter propagating geometry and have a waist radius of 600(10) µm. This part can be used for the ground state saturation spectroscopy as seen in fig. 5.1. For the Rydberg spectroscopy both beams are additionally overlapped with the infrared Rydberg laser, in this chapter referred to as coupling laser. The advantage of this setup is that for the Rydberg spectroscopy both the co- and counter propagating case can be investigated on photodiode PD_1 or PD_2 respectively, by simply blocking the other side arm of the probe laser or changing the orientation of the flip mirror. Since the signals are expected to be very small, they are measured using a lock-in amplifier. The working principle of this type of amplifier is to extract a signal oscillating with a known carrier frequency and thereby suppressing random noise effects. Therefore the coupling laser is modulated using the 0th order beam of an acousto optical modulator (AOM) with a frequency of roughly 80 kHz. The lenses l_1 and l_2 are used to first focus inside the AOM to reduce the switching time and subsequently modify the beam waist and accordingly the Rabi frequency, inside the cell.
For all following measurements in this part, if not stated otherwise, both lasers were locked on resonance, onto the actively stabilized transfer cavity using the cavity peak generated by the first order frequency modulation of the EOM. The frequency of the EOM was then increased or decreased in small steps (< 1 MHz) which the PID controller can follow, meaning the lasers can be slowly scanned while still being locked, where the EOM frequency also gives a relative frequency scaling. This technique also ensures that noise is sufficiently reduced by the lock-in amplifier, since long integration times, in the order of 50 ms, can be used.

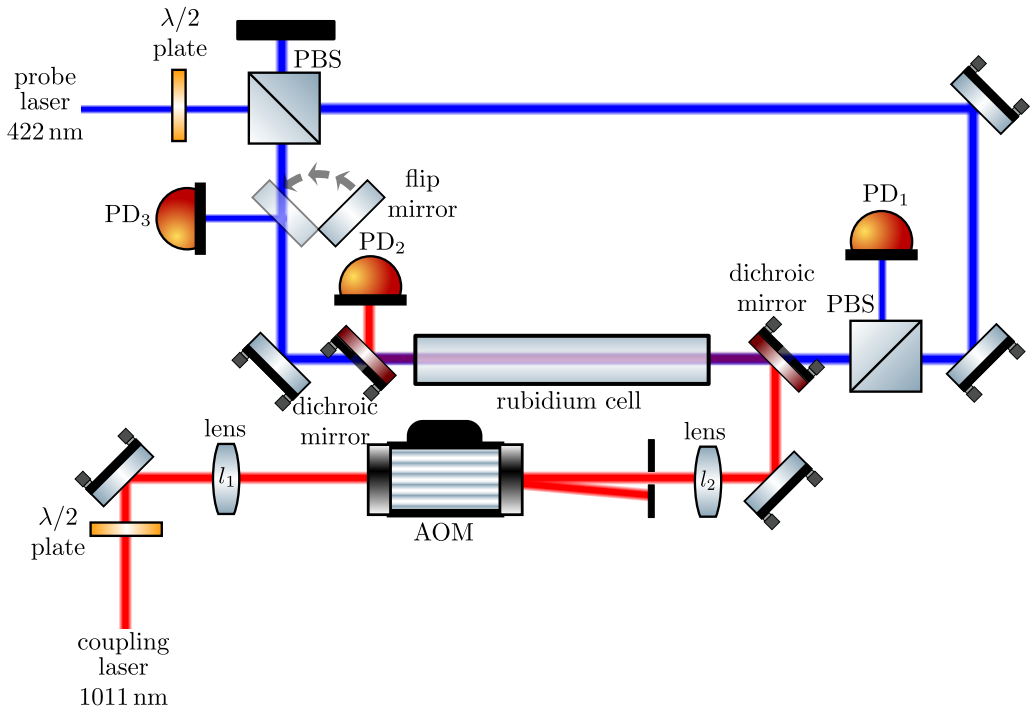

Figure 6.1: Schematic setup for the Rydberg spectroscopy.

7 Steady State Simulations

In order to not only get a feeling of what to expect, but to compare the results to the theory, it is necessary to also have simulations of the experiments. Those are based on the theoretical approach presented in chapter 1. Depending on the number n of atomic energy levels included in the simulation the n-dimensional Hamiltonian is set up with the corresponding Rabi frequencies and multi-photon detunings, as well as the Lindblad operator including all decay and dephasing rates. Putting those into the steady state Master equation in Lindblad form and solving the system of linear equations with the additional condition $\mathrm{Tr}(\rho) = 1$, a first result can already be obtained. But as mentioned before for experiments at or above room temperature the Doppler effect can not be neglected. Therefore, for each velocity class the density matrix has to be calculated individually, where the corresponding Doppler shift is included in the Hamiltonian. The determined results are then each weighted with the probability of the corresponding velocity class according to the Boltzmann distribution and summed up. To qualitatively compare them with measured results, in first approximation one can take the absorption coefficient of the corresponding transition which is proportional to the imaginary part of the susceptibility. This is the working principle for all simulations in this part.
With a simple three level system, the previous mentioned wavelength dependence of the EIT signal can be investigated. With two lasers in counter propagating geometry the calculated absorption coefficient can be seen in fig. 7.1. The upper row shows the obtained results per velocity class and in the lower row the resulting Doppler averaged signal can be seen, each for three different wavelength ratios between the probe and coupling laser, $\lambda_{12,\mathrm{a}}/\lambda_{23,\mathrm{a}} = 1000\,\mathrm{nm}/400\,\mathrm{nm} = 5/2$, $\lambda_{12,\mathrm{b}}/\lambda_{23,\mathrm{b}} = 400\,\mathrm{nm}/400\,\mathrm{nm} = 1$ and $\lambda_{12,\mathrm{c}}/\lambda_{23,\mathrm{c}} = 400\,\mathrm{nm}/1000\,\mathrm{nm} = 2/5$ for the subplots a) - c) correspondingly. The other parameters are identical for all simulations (Rabi frequencies, decays, temperature). In the velocity classes resolved simulations two features can be found in all three cases. First it can be seen that if the coupling laser is far off resonant, the probe only gets absorbed for a range of velocity classes (bright horizontal line around $v = 0$) and then stays in the intermediate state. This range is given by the Doppler width of the probe transition and thus proportional to $1/k_p$, which explains the broader feature for the first and the equal broadening for the second and third case. The second characteristic feature is the dark and narrow line at two-photon resonance. In the case of equal k vectors this occurs at $\Delta_{23} = 0$. In general the gradient of the line is given by $1/\left(k_p - k_c\right)$. Close to resonance the strong coupling laser perturbs the intermediate and excited state which leads to an avoided crossing. After weighting each velocity class with its according probability and summing over them the resulting transmission signal

can be seen in the lower row of fig. 7.1. For the second case with equal wavelengths the result is as expected a very narrow dip, because due to the counter propagating beams the Doppler broadening cancels out. For the other two cases the lineshape is not only given by the Doppler broadening but is dominated by the exact behavior of the avoided crossing. For longer probe wavelengths this leads, as seen in the lower left, to a very large and broad EIT feature and additional enhanced absorption caused by two-photon transitions at the wings. In contrast, if the wavelength of the coupling laser is longer, the EIT signal is strongly suppressed as seen in the lower right (note the different scaling of the y-axis compared to the other plots). Here the ratio of the two wavelengths is 0.4 while it is roughly 0.42 in the experiment. Accordingly, the EIT signal from a thermal vapor in the inverted scheme is expected to be weaker compared to the not inverted scheme.

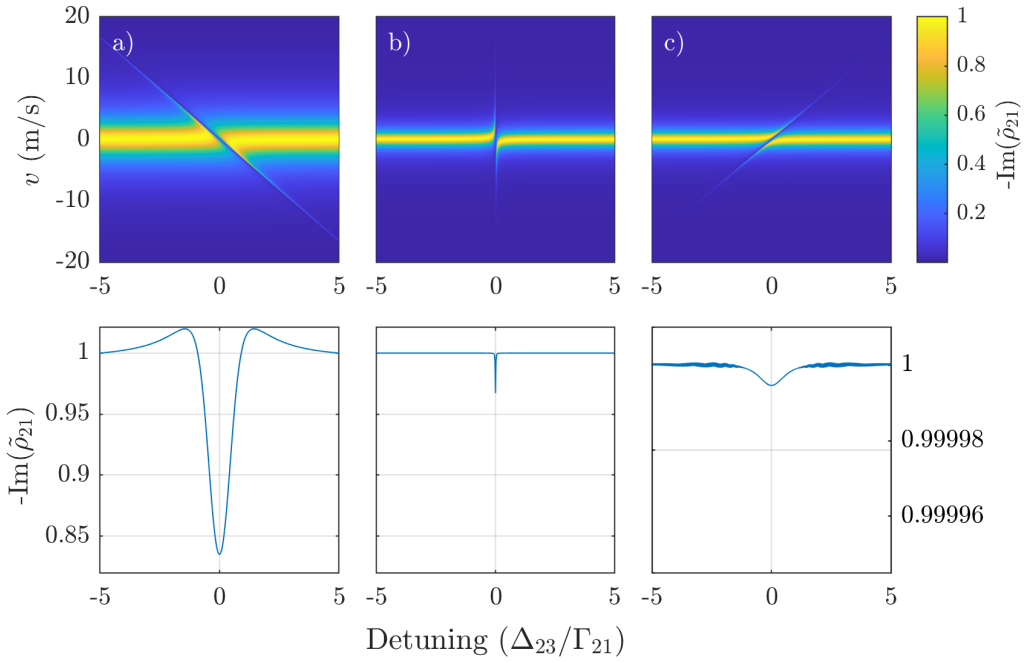

Figure 7.1: Simulated coherence between the ground and intermediate state $-\mathrm{Im}(\tilde{\rho}_{21})$ for different coupling detunings Δ_{23} and velocity classes v in the upper row and the resulting Doppler-averaged signal (lower row) in a three-level ladder system for counter propagating laser beams for different wavelength ratios of probe and coupling wavelengths: a) $\frac{\lambda_{12,\mathrm{a}}}{\lambda_{23,\mathrm{a}}} = \frac{1000\,\mathrm{nm}}{400\,\mathrm{nm}} = \frac{5}{2}$, b) $\frac{\lambda_{12,\mathrm{b}}}{\lambda_{23,\mathrm{b}}} = \frac{400\,\mathrm{nm}}{400\,\mathrm{nm}} = 1$ and c) $\frac{\lambda_{12,\mathrm{c}}}{\lambda_{23,\mathrm{c}}} = \frac{400\,\mathrm{nm}}{1000\,\mathrm{nm}} = \frac{2}{5}$. For all simulations: $\Omega_{12}/\Gamma_{21} = \frac{1}{500}$, $\Omega_{23}/\Gamma_{21} = \frac{2}{5}$, $\Gamma_{21} = 200 \cdot \Gamma_{32}$ and $T = 100\,^{\circ}\mathrm{C}$.

8 Experimental Results

8.1 Autler-Townes-Splitting

To observe Autler-Townes splitting in the classical way, e.g. [25], the strong coupling laser is used to induce the splitting, which is then measured with a coupling laser. Therefore, it is crucial that for the whole spatial probing area the splitting is equal, meaning the coupling power is constant. This can be achieved by accordingly choosing a larger beam diameter for the coupling laser and a more focused probe laser. But for this experiment the laser inducing the splitting is the probe laser itself, as the coupling between the Rydberg and intermediate state is very weak. This splitting can also be observed by probing the Rydberg transition. To be able to do this, one has to compromise and choose the beam waist of the coupling laser in the same order as the probe laser, with 700(20) µm, which means that one the one hand the splitting can be observed on both transitions, but the splitting is given by the average over all induced splittings in the probing area.
For high coupling and low probe frequencies the typical EIT signal can be clearly seen in fig. 8.1, but for increasing probe power the dip starts to split into two according to the Rabi frequency of the ground state transition. The splitting of the intermediate state can be directly observed, like theoretically derived in section 1.4.2. When neglecting an additional splitting of the excited state, the splitting is given by the effective two photon Rabi frequency $\Omega_{2,\mathrm{ph}} = \sqrt{\Omega_{12}^2 + \Omega_{23}^2}$, according to eq. (1.44).

In a simplified approach one can simulate this by assuming a three level system ($|1\rangle$ ground, $|2\rangle$ intermediate and $|3\rangle$ rydberg state). The Lindblad operator consists of three parts the direct decays between the levels $\Gamma_{\mathrm{dir},21}$ and $\Gamma_{\mathrm{dir},32}$ with the values from table 5.1 and 5.3, indirect decays to the ground state over other, not included dark states $\Gamma_{\mathrm{indir},21}$ and $\Gamma_{\mathrm{indir},31}$, as well as the transit time decays $\Gamma_{\mathrm{tt},31}$, $\Gamma_{\mathrm{tt},21}$ and $\Gamma_{\mathrm{tt},11}$. As the transit time decay is caused by atoms flying out of the excitation volume, which is here limited by the probe beam waist with $\omega_r = 600\,\mu$m, this rate is the same for all transitions and can be calculated using eq. (1.50) resulting in

$$\Gamma_{TT} = 0.066 \cdot 2\pi\,\mathrm{MHz}. \tag{8.1}$$

The values used for the indirect decays are calculated with [23] and can be found in appendix B. Here it was neglected that the atoms remain in other, not-included intermediate states for a finite time before they decay further into the ground state. For the remaining parameters (Rabi frequencies, temperature, detunings) the same values

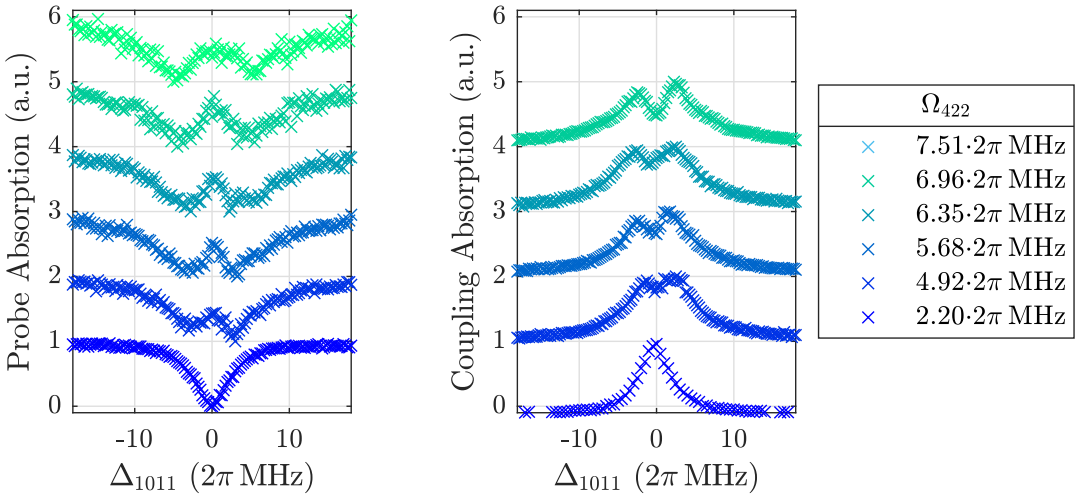

Figure 8.1: Measured probe and coupling transmission for different probe powers. The coupling laser was kept at a Rabi frequency of $1.28 \cdot 2\pi$ MHz and the cell at a temperature of 75 °C.

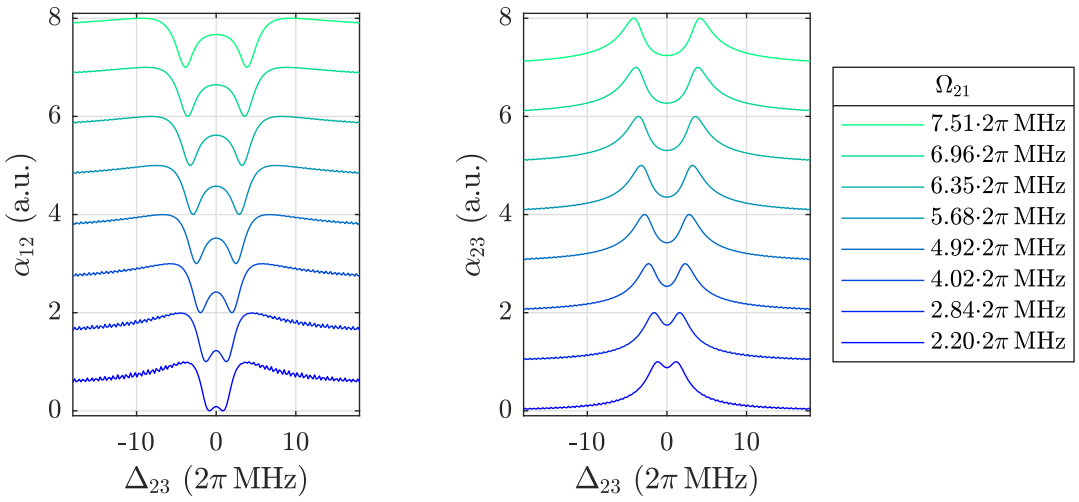

Figure 8.2: Simulated absorption coefficient for the ground state $\alpha 12$ and Rydberg transition α_{23} in dependence of the rydberg state detuning Δ_{23} for different ground state Rabi frequencies Ω_{21}. The temperature was set to 75 °C and the Rydberg Rabi frequency at $1.28 \cdot 2\pi$ MHz.

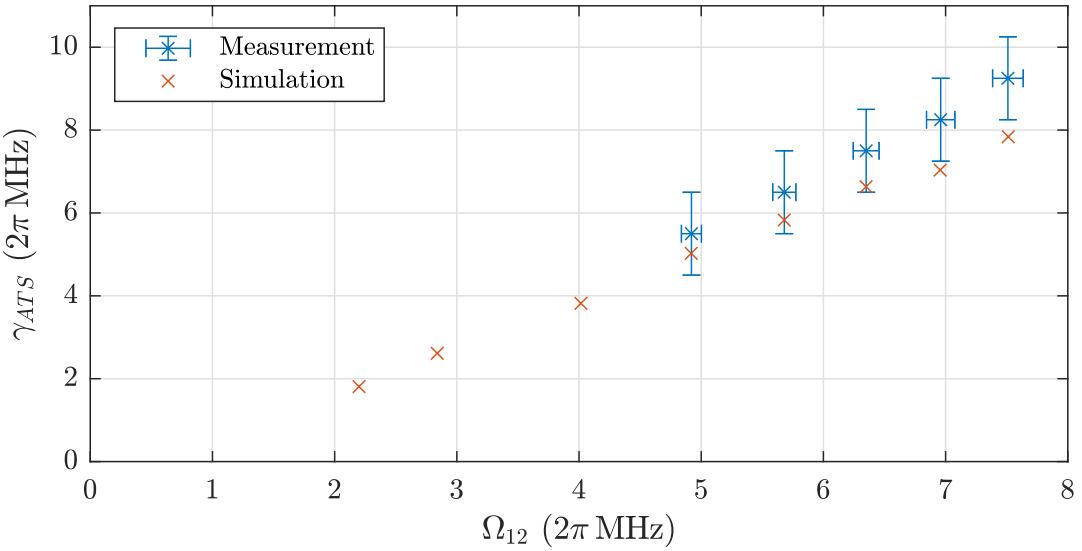

Figure 8.3: From the measurement and simulation extracted Autler Townes Splitting γ_{ATS} for different probe Rabi frequencies Ω_{12}. The coupling Rabi frequency was set to $1.28 \cdot 2\pi$ MHz and the cell temperature at 75 °C.

as in the experiment were chosen. The result can be seen in fig. 8.2. The fast additional oscillations, which can be seen on the wings of the signal are a sampling feature caused by the discrete selection of velocity classes and can be reduced by increasing the number of velocity classes taken into account.
Qualitatively, the signal shape and behavior of the measurement can be reproduced very well. In order to quantitatively compare the experimental results with the simulations, from both the corresponding Autler Townes splittings γ_{ATS} are abstracted. As seen in fig. 8.3 the measured splitting is always larger than the simulated one but in the same order of magnitude. The difference in the experimental data can be attributed to the uncertainty of the Rabi frequencies, that is namely influenced by the beam waist and laser power, additionally the measured splitting can be distorted by the drifting of the transfer cavity, caused by temperature or pressure changes. In addition the fitting of the Gaussian peaks are also subject to errors, which is shown by the corresponding errorbars. Those are all summarized in the error bars displayed with the results. Furthermore, only a very simplified model of the actual level system is assumed in the simulation, neglecting additional states or interactions and additionally, all spacial properties of the laser beams like the divergence in propagation direction or the Gaussian beam profile are not included.

8.2 Electromagnetically Induced Transparency

To further investigate the behavior of EIT in the inverted scheme the coupling laser was focused down to a waist radius of 160(10) µm, to achieve higher Rabi frequencies. For all following measurements the cell was kept at a temperature of 115 °C, the ground state laser was locked to the ^{85}Rb $5S_{1/2}$ $F = 3 \rightarrow 6P_{1/2}$ $F' = 3$ transition and the coupling laser to the corresponding Rydberg transition $6P_{1/2}$ $F' = 3 \rightarrow 40S_{1/2}$.

8.2.1 Observed Hyperfine Splitting

Even though the probe laser is locked to the $F' = 3$ intermediate hyperfine state, due to the Doppler broadening of the atoms inside the cell, for a certain velocity class v the Doppler detuning of the probe laser is equal to the hyperfine splitting Δ_{HFS} of the $6P_{1/2}$ state

$$\Delta_{\mathrm{HFS}} = k_{12} \cdot v \tag{8.2}$$

with the probe wavevector k_{12}, meaning the excitation is on resonance to the $F' = 2$ intermediate state. To excite the atoms of this velocity class also to the Rydberg state the coupling laser has to be detuned accordingly depending on whether the lasers are co- or counter-propagating. By scanning the coupling laser this effective hyperfine splitting $\Delta_{\mathrm{HFS'}}$ can be measured

$$\begin{aligned} \Delta_{\mathrm{HFS'}} &= k_{12} \cdot v \pm k_{23} \cdot v \\ &= \Delta_{\mathrm{HFS}} \left(1 \pm \frac{k_{23}}{k_{12}}\right) \\ &= \Delta_{\mathrm{HFS}} \left(1 \pm \frac{\lambda_{12}}{\lambda_{23}}\right) \end{aligned} \tag{8.3}$$

here the positive sign corresponds to co- and the negative sign to counter-propagating beams.
Figure 8.4 shows the measured EIT-signal for both cases. By fitting a Gaussian profile to the absorption peaks the splitting can be calculated. The obtained values can be compared to the, with eq. (8.3) calculated, theoretical values. For those a hyperfine splitting of $117.33 \cdot 2\pi$ MHz [22] is assumed. The obtained values are shown in table 8.1.

Table 8.1: Comparison of the theoretical and measured splittings between the two intermediate states $6P_{1/2}$ $F' = 2$ and $F' = 3$ $\Delta_{\mathrm{HFS'}}$ for co- and counter-propagating laser beams. For the hyperfine splitting $117.33 \cdot 2\pi$ MHz [22] is assumed.

	$\Delta_{\mathrm{HFS'},\,\mathrm{theo}}$ $(2\pi\,\mathrm{MHz})$	$\Delta_{\mathrm{HFS'},\,\mathrm{meas}}$ $(2\pi\,\mathrm{MHz})$
co-propagating	166.29	165.29(260)
counter-propagating	68.37	68.52(190)

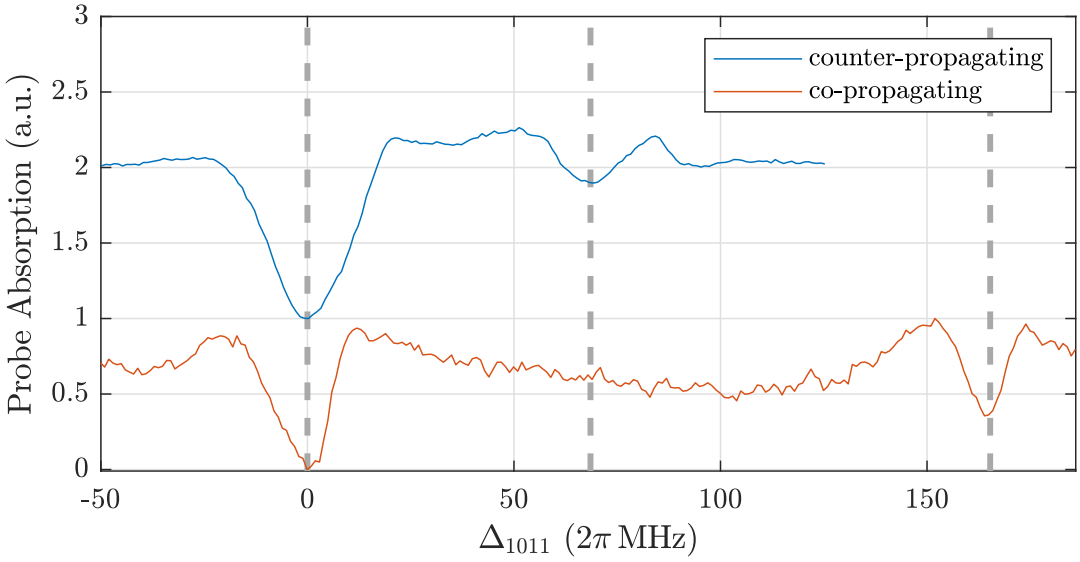

Figure 8.4: Measured probe absorption in dependence of the coupling detuning Δ_{1011} for the lasers in co- and counter-propagating configuration. In both cases the coupling Rabi frequency was $6.07 \cdot 2\pi$ MHz and the probe frequency $7.78 \cdot 2\pi$ MHz in the co-propagating and $7.51 \cdot 2\pi$ MHz in the counter-propagating case. Marked by the gray dashed lines are the center of the fitted absorption dips.

It can be seen that the measured values are in good agreement with the theoretical values. For co-propagating lasers the EIT-signal is weaker due to the Doppler averaging, which is the reason for the worse signal to noise ratio and the resulting greater deviation from the theoretical value.

8.2.2 Power Dependency

To further investigate the behavior of the EIT-signal, systematic measurements were performed for different probe and coupling Rabi frequencies, by changing the corresponding laser power.

Counter-Propagating

Figure 8.5 shows the obtained signal for different probe Rabi frequencies for counter-propagating lasers. On the left side, the unmodified results are shown, whereas on the right side, the data sets have been individually normalized. The most prominent feature is that for certain frequencies the prominence of the EIT-dip not only decreases but also changes sign and turns into a peak. This behavior was also observed in a similar level scheme using cesium [24]. The changing point from dip to peak is also different for the two hyperfine intermediate states. For the $F' = 2$ transition one can clearly see the EIT dip starting to appear but only at higher Rabi frequencies compared to the $F' = 3$ transition. It is also important to note, that the stated probe Rabi frequencies are calculated using the reduced dipole moment $\langle J| \, |e\boldsymbol{r}| \, |J'\rangle$, so in order to calculate the Rabi frequency for the specific hyperfine transitions this value has to be weighted according to eq. (1.23) with the corresponding transition strength factor $\sqrt{S_{FF'}}$. This supports the intuitive idea, that the different tipping points are connected to the corresponding transition strength factors, as $S_{33} < S_{32}$. This behavior change of the signal can be explained by two competing phenomena, enhanced transmission (EIT) and enhanced absorption (EA), with one of them dominating depending on the Rabi frequencies. For constant coupling power the transition from EIT to EA takes place for decreasing probe Rabi frequencies. A possible explanation for this is that EIT is a phase sensitive process, whereas EA is not. This means that a dephasing faster than the Rabi frequencies would make it impossible to observe EIT but not influence EA. Since dephasing processes often depend on the velocity of the atoms, this would also explain the difference between the two intermediate hyperfine states. However, to confirm this theory, further measurements and detailed theoretical studies are necessary.
It can also be seen that for increasing probe intensities the EIT feature gets broader, which can be attributed to an Autler-Townes splitting. But in contrast to the previous section, here, the other occurring effects are more prominent, and overlay the splitting which therefore cannot be resolved.
For a higher coupling Rabi frequency and increasing probe power (lower left of fig. 8.5),

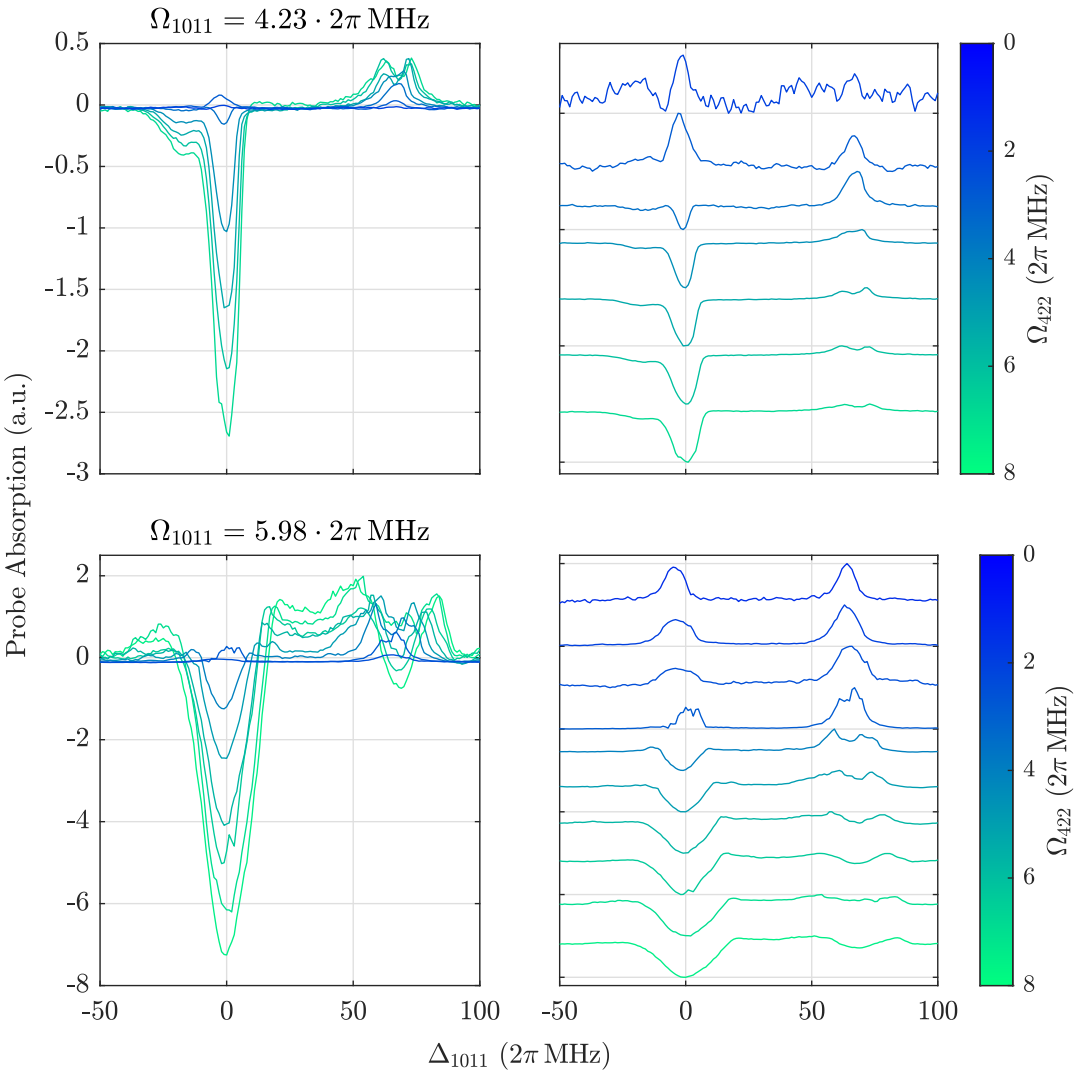

Figure 8.5: Measured probe absorption signal for counter-propagating beams and different probe Rabi frequencies in dependence of the coupling detuning. The left side shows the unmodified measurement results, whereas on the right side they are individually normalized and plotted in a waterfall-like fashion.

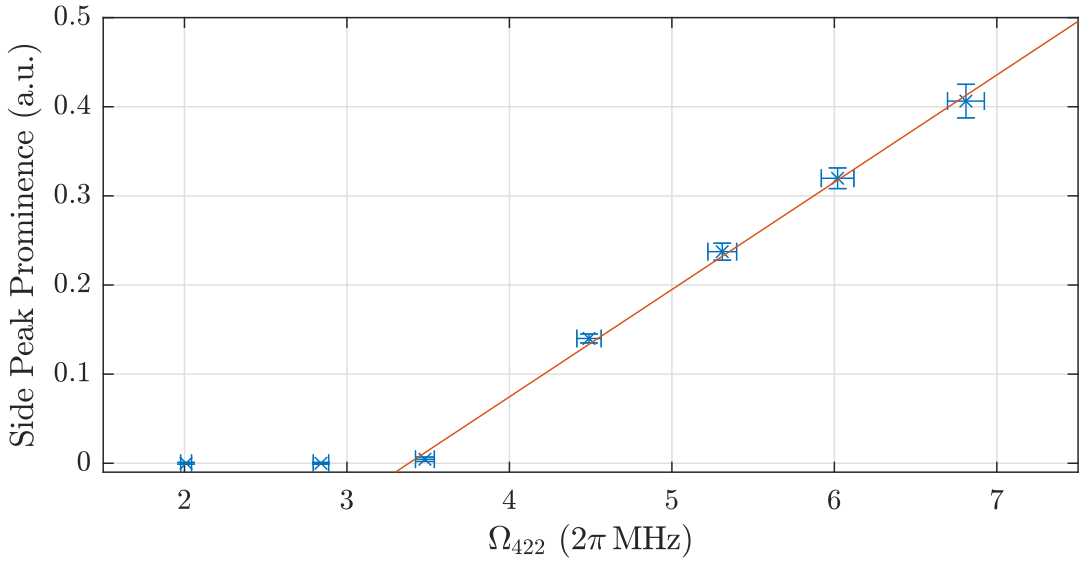

Figure 8.6: Measured prominence of the side peak for different probe Rabi frequencies and a coupling frequency of $4.23 \cdot 2\pi$ MHz, as well as a first degree polynomial fit function, fitted to the data points with $\Omega_{422} > 3 \cdot 2\pi$ MHz.

the enhanced absorption on the wings of the EIT signal can be seen. Between the two hyperfine signals they overlap leading to the effect, that the intensity does not go back to zero.
Another feature visible in the upper left part of fig. 8.5 is that for increasing probe Rabi frequencies a side peak emerges from the main EIT peak towards negative coupling detungings, corresponding to lower energies. As Rydberg-Rydberg interactions for S-states are always repulsive, those would lead to a feature towards positive detunings and can therefore not be the underlying effect causing the side peak. An attractive force and thus possible reason is the DC-Stark effect. In general, an external electric field induces a dipole moment inside the atom, leading to a change in the energy levels, the so called Stark-shift Δ_{Stark}. The size of the shift depends on the polarizability of the atom α and the electric field E and is given by

$$\Delta_{\mathrm{Stark}} = -\frac{1}{2}\alpha E^2 \tag{8.4}$$

for small electric fields, which cannot break the degeneracy of the angular momentum quantum number [26]. In order to examine the cause of this electric field, a Gaussian profile if fitted to the side peak and the obtained prominence is plotted over the corresponding probe Rabi frequency in fig. 8.6. Here, a clear threshold can be seen, after with the prominence of the side peak increases proportional with the Rabi frequency. This behavior indicates, that the electric field inducing the Stark effect is due to the creation of a plasma like investigated in [27]. The observation of the linear scaling with the probe Rabi frequency also matches the results from [27], as for this data set the coupling laser

was scanned from high to low detunings.
In fig. 8.7 the measured signal for different coupling Rabi frequencies is shown. For the on resonance transition it can be seen, that in the case of the investigated probe intensities the coupling laser is not able to induce the change from EIT to EA. The off resonant transition shows the beginning of the transition from EA to EIT for increasing coupling Rabi frequencies.
Furthermore it can be seen, that higher coupling Rabi frequencies not only increase the prominence of the EIT dip but also lead to a broadening of the feature. This effect occurs due to saturation, which reduces the absorption near the resonance more than for frequencies far off-resonant. The absorption coefficient is Lorentzian shaped and has a full-width at half maximum Γ of [28]

$$\Gamma = \sqrt{2\Omega^2 + \Gamma_0^2} \tag{8.5}$$

with the natural linewidth Γ_0 and the Rabi frequency Ω inducing the so called power broadening. In first approximation fitting a Lorentzian profile to the main EIT dip of the data in fig. 8.7 and extracting the corresponding FWHM can be used to compare the measurements to the theory. The obtained broadenings for different coupling frequencies and two different probe frequencies can be seen in fig. 8.8, as well as the fitted theoretical behavior according to eq. (8.5). In direct comparison, it is noticeable, that there is an offset between the two measurement series and the case with a lower probe Rabi frequency matches the theory better. The offset shows the additional broadening caused by the probe laser. For the Lorentzian fit the data points in the detuning range of the side peak were neglected but for high coupling and probe Rabi frequencies the two peaks start to overlap which also leads to a broadening of the EIT dip not included in the previous theoretical model explaining the higher derivation of the second data set. Also not included is the broadening by a beginning Autler-Townes splitting. The fitting parameter Γ_0 does not resemble the natural linewidth but the combined linewidth resulting from all additionally occurring broadening effects e.g. Doppler broadening. The obtained values for the probe Rabi frequency of $4.49 \cdot 2\pi\,\mathrm{MHz}$, $\Gamma_{0,1}$ and $\Gamma_{0,2}$ for $6.35 \cdot 2\pi\,\mathrm{MHz}$ are

$$\Gamma_{0,1} = 4.20(87) \cdot 2\pi\,\mathrm{MHz} \tag{8.6}$$

$$\Gamma_{0,2} = 6.94(147) \cdot 2\pi\,\mathrm{MHz} \tag{8.7}$$

and in the expected order of magnitude.

Co-Propagating

The same systematic analysis of the power dependency of the EIT- and EA-signal can also be done with co-propagating laser beams. This is shown in fig. 8.9. Compared to the counter-propagating case, for increasing probe power an Autler-Townes splitting of the EA peak can be seen for both hyperfine transitions. For increasing coupling Rabi frequencies however, this splitting does not significantly increase.

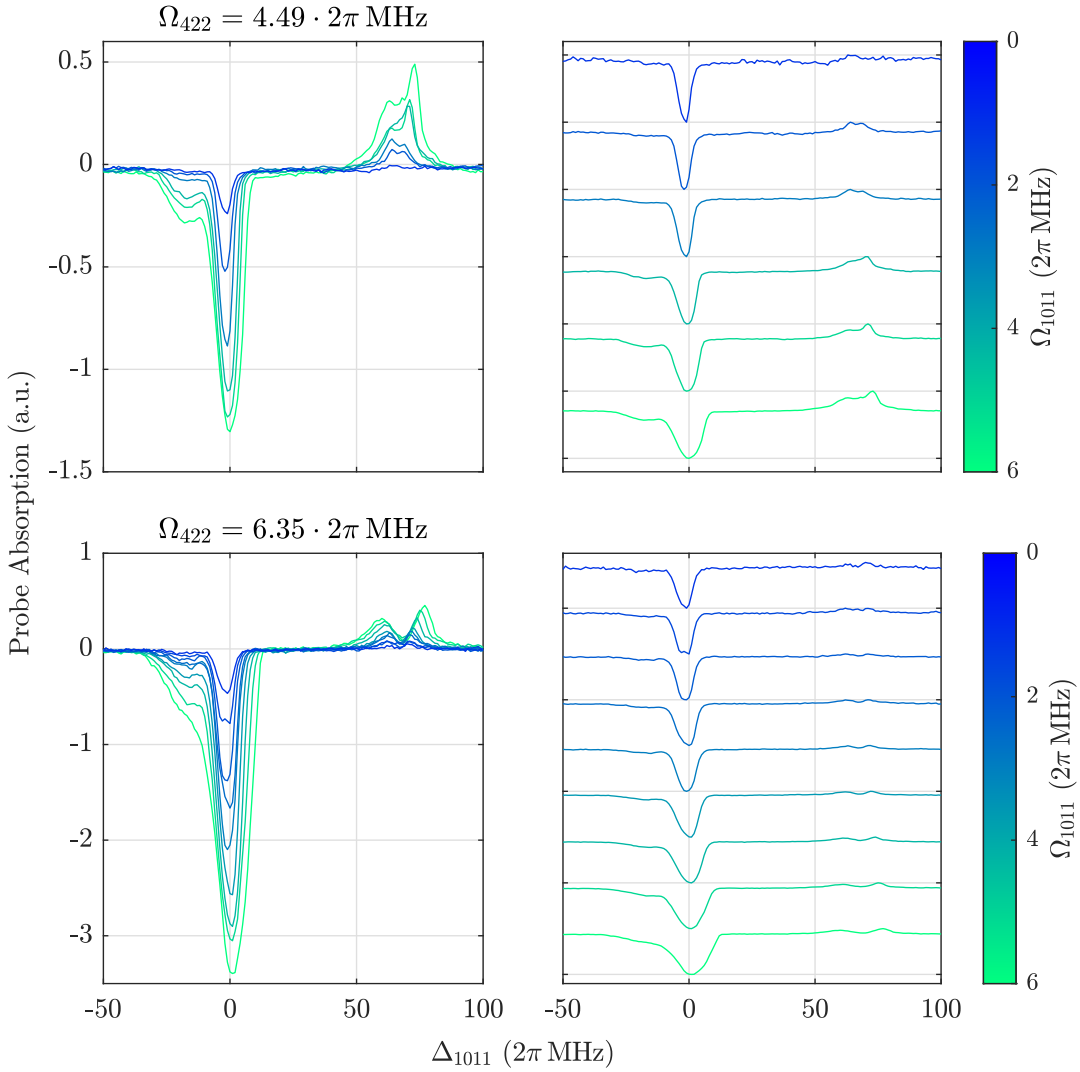

Figure 8.7: Measured probe absorption signal for counter-propagating beams and different coupling Rabi frequencies in dependence of the coupling detuning. The left side shows the unmodified measurement results, whereas on the right side they are individually normalized and plotted in a waterfall-like fashion.

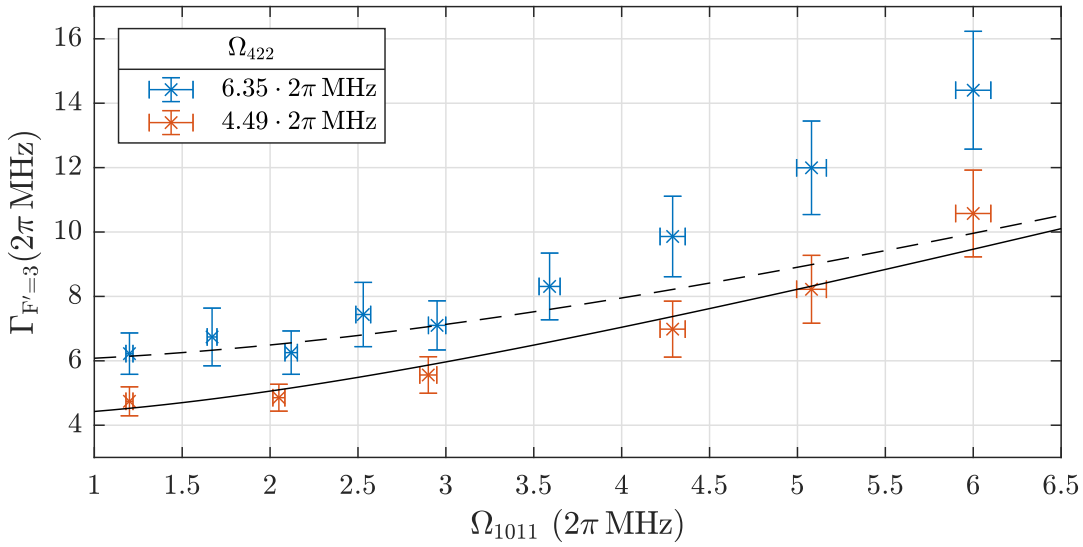

Figure 8.8: Linewidth $\Gamma_{F'=3}$ of the EIT-signal from the ^{85}Rb $5S_{1/2}$ $F = 3 \rightarrow 6P_{1/2}$ $F' = 3$ $\rightarrow 40S_{1/2}$ transition for different coupling Rabi frequencies Ω_{1011}, obtained by fitting a Lorentzian profile. The measurements are fitted with a theoretical model for power broadening $\Gamma = \sqrt{2\Omega^2 + \Gamma_0^2}$ shown in a solid black line for the red data points and dashed lines for the blue data points.

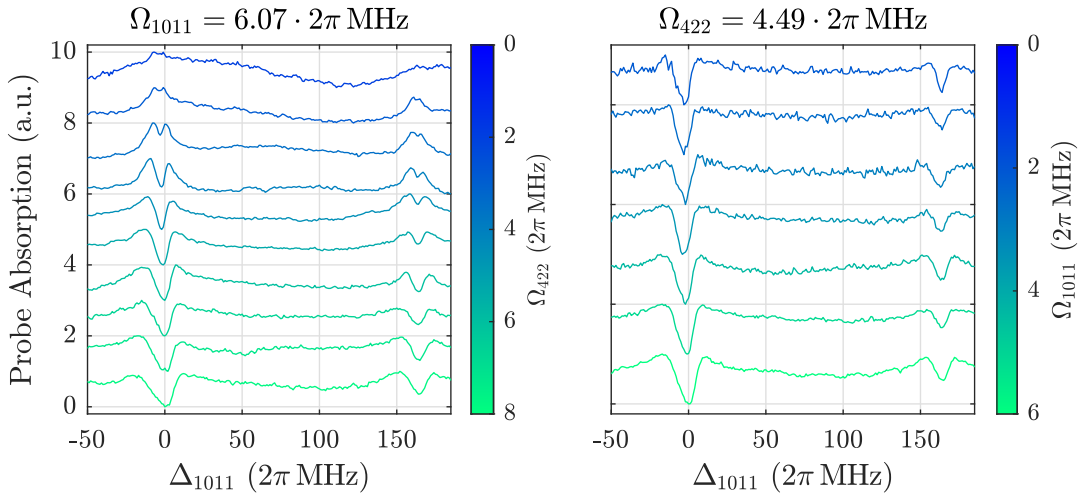

Figure 8.9: Measured probe absorption signal for co-propagating beams in dependence of the coupling detuning for different probe and coupling Rabi frequencies. The measurement result are individually normalized and plotted in a waterfall-like fashion.

8.2.3 Simulations

To further investigate and understand the, in this system occurring, effects like enhanced transmission and enhanced absorption or Autler-Townes splitting simulations are needed. But therefore it if not sufficient enough to assume a three or for level system, as also the optical pumping of other, not by laser fields coupled, intermediate states plays an important role. A first approximation would be to include one additional state for every coupled level. When including all hyperfine states (in total 6 states) this would mean solving the Lindblad equation for a 12-level system, which was out of scope for this thesis.

Part IV

Thermal Nanosecond Pulsed Rydberg Spectroscopy

Introduction

Observing coherent Rydberg dynamics in the form of Rabi oscillations is more challenging in thermal vapors compared to ultra cold experiments, due to the short coherence time given by the velocity distribution of the atoms. As this timescale can also not be easily extended the only possibility is inducing dynamics faster than the decoherence time, in this case in the order of one gigahertz.

The excitation to the Rydberg state in this experiment is also done via a three-level ladder system as shown in fig. 8.10. But in contrast to the experiment discussed in part III, here the Rydberg transition was changed to excite the $32S_{1/2}$ state. This has multiple reasons the most important one is the nearly 1.5 times larger transition dipole moment compared to the $40S_{1/2}$ state (see table 5.3), which means that with the same laser parameters (power and beam waist) the Rabi frequency is also 1.5 times larger. Additionally a dephasing of the Rydberg state of rubidium has been observed [29], which scales, like the Van der Waals interaction, with $(n^*)^{11/2}$ and dampens the Rabi oscillations.

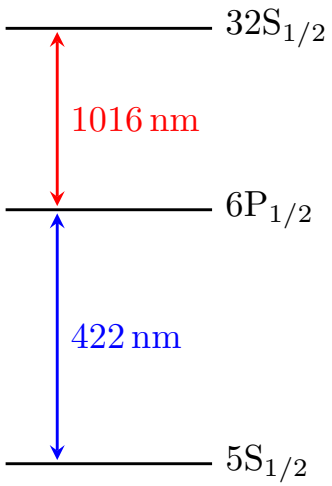

Figure 8.10: Excitation scheme used for the pulsed Rydberg spectroscopy.

9 Experimental Setup

In order to achieve high Rabi frequencies for a certain transition there are two parameters one can optimize. Either increase the laser power or decrease the beam waist. For the Rydberg transition both things are needed due to the small dipole moment. By using the pulsed fiber amplifier (described in section 5.2.1) a peak power of 100 W can be provided and the beam is additionally tightly focused into the cell, with a focal radius of around 35 μm. The ground state probe laser is kept continuous, but has also to be tightly focused to at least half the beam size of the coupling laser, to ensure that in the probing area the coupling Rabi frequency is homogeneous.
In fig. 9.1 the complete experimental setup can be seen. The 422 nm probe laser and 1016 nm coupling laser are overlapped inside a 5 mm rubidium cell in counter propagating configuration using dichroic mirrors and individually focused inside the cell. The first photodiode PD_1 is used to monitor the pulses and as an optical trigger. With PD_2, an AC-coupled photodiode from Femto with a bandwidth from 10 kHz to 1.4 GHz, the transmission signal is measured.
To determine the exact focus size of both lasers, the cell was first replaced with a pinhole with a diameter of 10 μm which was moved through the focus in horizontal and vertical direction and the transmitted intensities of the two lasers were measured individually. The obtained signals in horizontal direction can be seen in Figure 9.2. This signal does not directly correspond to the beam profile but the convolution of the beam and pinhole shape. Therefore this convolution is fitted to the data and the obtained focus radii are

$$w_{r,422} = 17.03(150)\,\mu\text{m} \tag{9.1}$$

$$w_{r,1016} = 37.35(65)\,\mu\text{m}. \tag{9.2}$$

Measurements for the vertical axis yielded results included in this uncertainty range. For tightly focused beams the problem arises, that they are more divergent along the propagation axis. The quantity used to measure this is the Rayleigh length z_R, which is defined as the distance from the minimum beam waist $w_{r,0}$ to where the beam radius is increased by a factor of $\sqrt{2}$

$$z_\text{R} = \frac{\pi w_{r,0}^2}{\lambda}. \tag{9.3}$$

As for these experiments it is important, to have a homogeneous Rabi frequency along the propagation axis, therefore half the cell length has to be in the same order of magnitude as the Rayleigh length. Therefore a 5 mm cell was chosen. To obtain high enough rubidium densities, the reservoir of the cell was heated to 130 °C and additionally, to

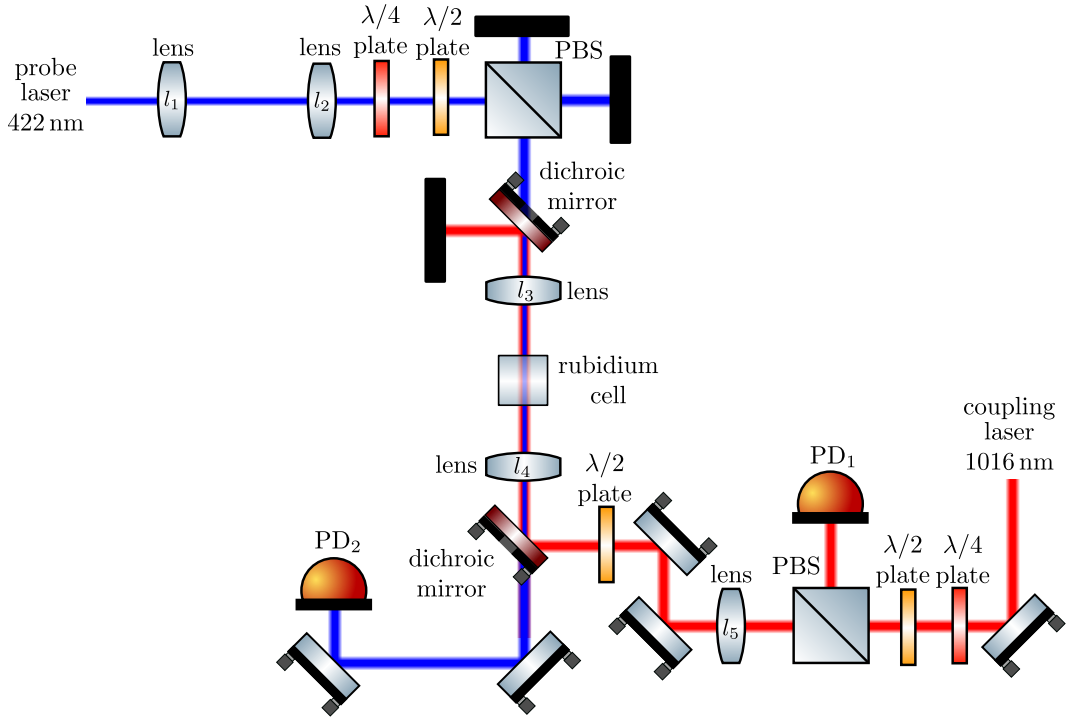

Figure 9.1: Schematic setup for the pulsed Rydberg spectroscopy to measure Rabi oscillations.

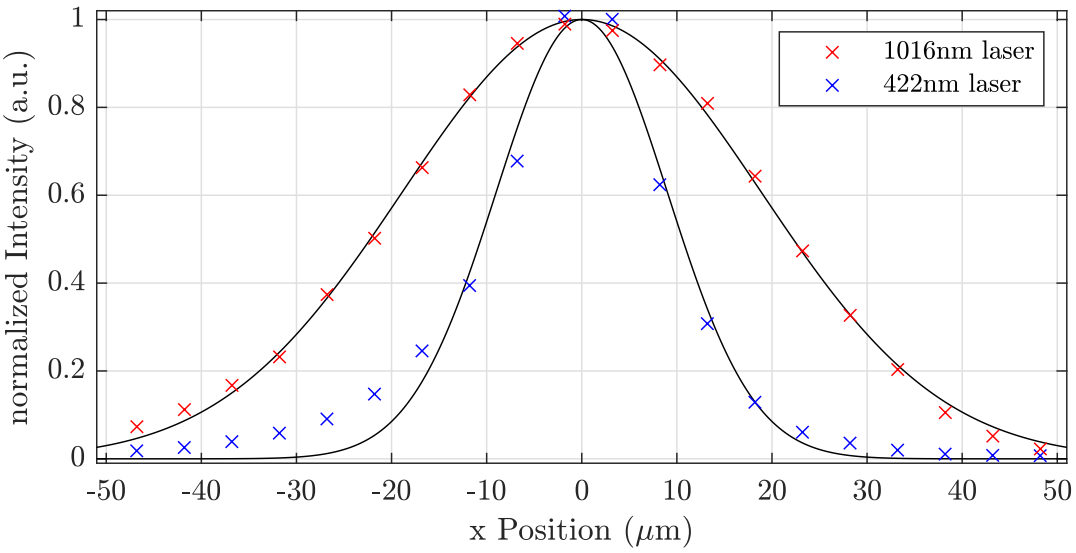

Figure 9.2: Measured intensity for the blue probe and infrared coupling beam in dependence of the position of a 10 μm pinhole moving horizontally through the beam, as well as the fitted convolution of the pinhole and Gaussian shaped beam profile. The obtained focus radii are 17.03(150) µm and 37.35(65) µm for the probe and coupling beam respectively.

ensure that no rubidium condensates to the cell windows, where the laser beams pass trough this part was heated to 150 °C. This temperature however, does not change the vapor pressure in the cell, but determines the velocity distribution.

10 Time Dependent Simulations

In the case of pulsed excitations on the nanosecond timescale, it is not sufficient to calculate the steady state solution, as this regime is only reached for long timescales with respect to the occurring decay and dephasing rates, which are also in the nano-/microsecond range. Therefore, the time dependent Master equation has to be solved, which will be done numerically by using the Runge-Kutta method. The coupled system of differential equations is set up in the same way as described in chapter 7, also including the Doppler effect. To solve differential equations, additionally an initial condition is needed, which is determined by the exact system itself. For all experiments discussed here the probe laser, driving the ground state transition, is continuous waved so the initial condition before the Rydberg pulse arrives is thus given by the steady state solution of the two-level system consisting of the ground and excited state coupled by the probe laser and can be calculated using eq. (1.30).

As previously stated, the goal of this experiment is to measure the Rydberg Rabi oscillations by probing the ground state transition. In order to understand the working principle of this and illustrate the dynamics of such a system the three-level system from fig. 8.10 is simulated. The assumed decays can be found in appendix B, for simplicity reasons only the natural lifetime of the excited states are considered. For the coupling laser a rectangular pulse shape with a pulselength of 10 ns and a Rabi frequency of $500 \cdot 2\pi$ MHz was chosen. Figure 10.1 shows the resulting time evolution of the populations (top) and coherences (bottom). The gray dashed lines mark the beginning and end of the pulse. The dynamics of the system can be separated in three parts, before, during and after the coupling pulse.

Before the coupling pulse arrives, the only present light field is the continuous waved probe laser, here with a Rabi frequency of $25 \cdot 2\pi$ MHz, coupling the ground $|1\rangle$ and intermediate state $|2\rangle$. Therefore, no atom can be excited in the Rydberg state $|3\rangle$, and the system can be described as a two-level system in the steady state regime. This is the initial condition for the simulations. Due to the weak probe Rabi frequency more than 96 % of the population stays in the ground state and correspondingly less than 4 % end up in the intermediate state, resulting in a coherence $\mathrm{Im}(\tilde{\rho}_{21})$ close to zero. As expected those properties stay constant for $t < 0$ as no additional effect arises which could disturb the steady state.

At $t = 0$ the pulse arrives and accordingly the coupling Rabi frequency starts to in-

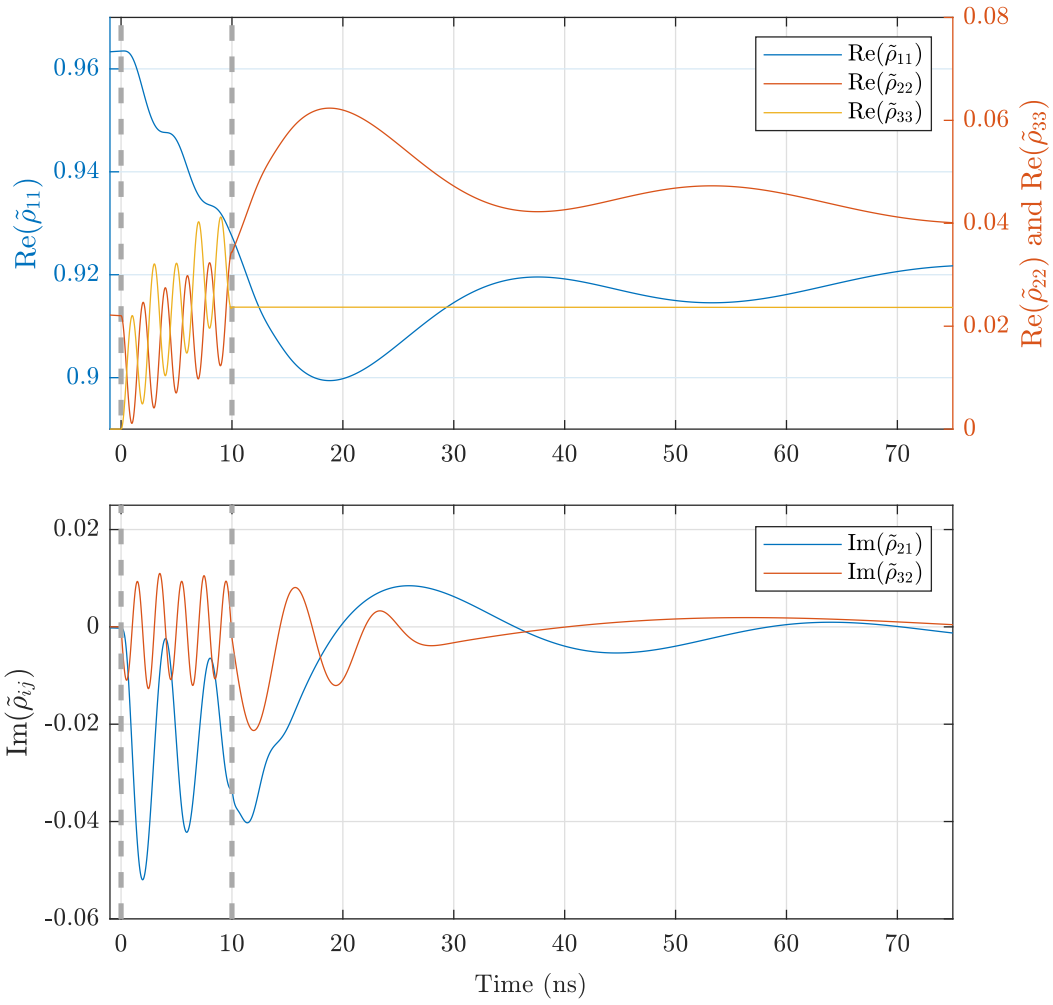

Figure 10.1: Simulated populations and coherences for a three level system of the $5S_{1/2} \rightarrow 6P_{1/2} \rightarrow 32S_{1/2}$ transition with counter propagating laser beams, the corresponding decays (see appendix B) and a temperature of 155 °C. The assumed coupling and probe Rabi frequencies are $500 \cdot 2\pi$ MHz and $25 \cdot 2\pi$ MHz respectively. The probe laser is continuous wave and the coupling laser pulsed, whereby a rectangular pulseshape and duration of 10 ns is assumed. The gray dashed lines mark the beginning and end of the pulse.

crease, the previous steady state is disturbed as population from the intermediate state gets pumped into the Rydberg state. After a so called π pulse, with $\Omega t = \pi$, in this case at 1 ns, nearly all population previously in the intermediate state has been moved to the Rydberg state. As the population decreases in the intermediate state, it gets refilled with atoms from the ground state, leading to an increasing average population in the intermediate and Rydberg state per Rabi cycle. The coherence between the two states $\mathrm{Im}(\tilde{\rho}_{32})$ shows oscillations with the same frequency. The coherence between ground and intermediate state however shows oscillations with only half the frequency. In order to explain this, it is helpful to transform the system into the dressed state picture as described in section 1.4.2, where the splitting of the eigenstates directly corresponds to the oscillation frequency occurring between those. On resonance, the splitting between $|+\rangle$ and $|-\rangle$, which are given by the superposition of the intermediate $|2\rangle$ and excited state $|3\rangle$, is $\sqrt{\Omega_{12}^2 + \Omega_{23}^2} \approx \Omega_{23}$. The energy of the ground state zero in the dressed state picture, in first approximation for $\Omega_{12} \approx 0$. Therefore the splitting between $|0\rangle$ and $|-\rangle$ is $\frac{1}{2}\sqrt{\Omega_{12}^2 + \Omega_{23}^2} \approx \frac{1}{2}\Omega_{23}$, which matches the simulation results. In a more visual explanation of the factor $\frac{1}{2}$ one can think of the Bloch sphere [28]. In a two level system, a π pulse with $\Omega t = \pi$ flips all population from the ground to the excited state, but also adds the factor i to the phase. This means that after one Rabi oscillation (2π pulse) all population is back in the ground state but the phase is inverted. Therefore, to restore the population and phase in the initial value two Rabi cycles are needed. Since coherences are phase sensitive, the oscillations between ground and intermediate state have a frequency of exactly half the coupling frequency between the intermediate and Rydberg state.
If the coupling Rabi frequency would remain constant the system would reach a new steady state, which however is not the case on the nanosecond timescale.

With the end of the coupling pulse at $t = 10$ ns the dynamics of the system change once more. As the coupling Rabi frequency is zero, the atoms in the Rydberg state at the end of the pulse remain there and slowly decay back to the intermediate and ground state. But as the lifetime of the $32S_{1/2}$ Rydberg state is roughly 30 μs this can be neglected on the nanosecond timescale. The population remaining in the Rydberg state depends on the exact point in the Rabi cycle at which the pulse ends. Without the coupling laser the dominating driving force in the system is the probe laser. The system can again be described as a two level system, like before the pulse, where the total population is not 1 but $1 - \tilde{\rho}_{33}(t = 10)$. The exact behavior of the population and coherence of the two-level system depend solely on the density matrix in the moment the pulse end, as this sets the starting values for the following dynamics. The system will reach an approximate steady state solution again on the hundred nanosecond timescale. However, the actual steady state is only reached once all Rydberg atoms have decayed back into the ground or intermediate state. This will then also equal the initial starting point before the coupling pulse $\tilde{\rho}(t = 0) = \tilde{\rho}(t \to \infty)$.
For the following experiments in this part, due to the finite beam sizes, the dominating

effect for the decay will be the transit time, meaning the Rydberg atoms fly out of the probe area, which will reduce the effective lifetime to below 100 ns. The repetition rate of the pulses is 100 kHz, corresponding to a pulse every 10 μs, which means that it can be assumed that on this timescale the initial steady state is restored.

Those calculations and observations however, are only valid if the probe laser is weak in comparison the the occurring decay rates and can be neglected on the timescale of the pulse. Figure 10.2 shows the coherences for two different probe Rabi frequencies and a coupling Rabi frequency of $1000 \cdot 2\pi$ MHz. In the upper plot a) the previously discussed case for a weak probe laser with a Rabi frequency of $10 \cdot 2\pi$ MHz is shown again and in the lower plot b) the probe Rabi frequency is $100 \cdot 2\pi$ MHz. In comparison it becomes noticeable that for the coherence $\mathrm{Im}(\tilde{\rho}_{32})$ the oscillation frequency is increased slightly (see different phase of oscillation at the end of the coupling pulse), like predicted in the dressed state picture where the oscillation frequency is given by $\sqrt{\Omega_{12}^2 + \Omega_{23}^2}$. Also the probe frequency leads to a respective amplitude modulation of the signal. In the coherence between ground and intermediate state the effect of a stronger probe laser is more significant. The probe Rabi frequency superimposes the actual signal and the overlap of both frequencies is measured. On the other hand, when comparing the absolute values the maximum amplitude in case b) is more than five times stronger than in case a).

In summary, from the simulations, the best way to directly measure Rydberg Rabi oscillations is with a weak probe laser and very strong coupling laser. But, as a weak probe laser corresponds to less Rydberg atoms this would mean an accordingly weaker signal which is more challenging to actually measure. Therefore, for the experiment a compromise between these two has to be found, so that the signal can be measured with the given technical means, but the probe Rabi frequency does not superimpose the actual signal.

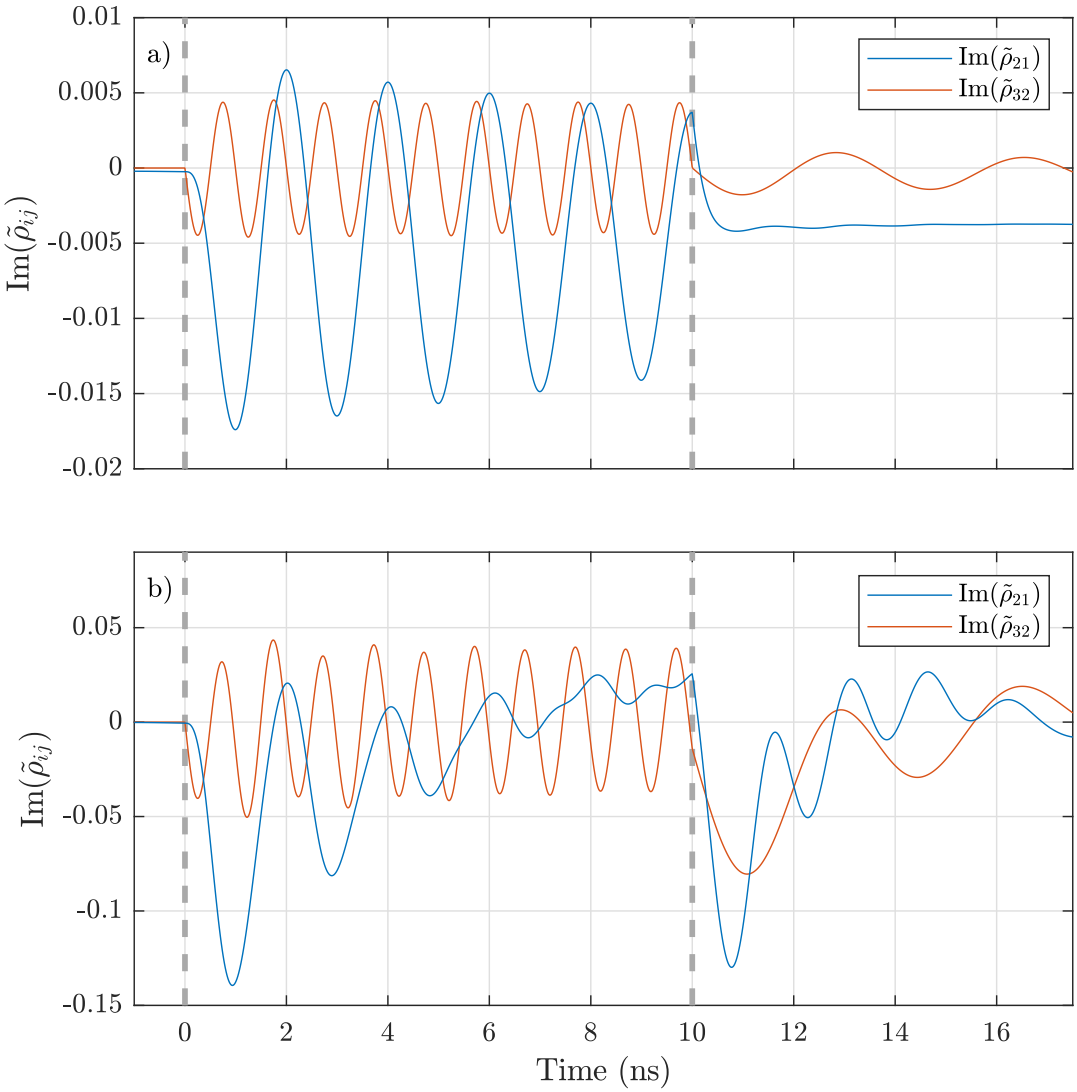

Figure 10.2: Simulated coherences for a three level system of the $5S_{1/2} \rightarrow 6P_{1/2} \rightarrow 32S_{1/2}$ transition with counter propagating laser beams, the corresponding decays (see appendix B) and a temperature of 155 °C. The assumed coupling Rabi frequency is $1000 \cdot 2\pi$ MHz and the probe Rabi frequency for the upper plot a) $10 \cdot 2\pi$ MHz and for the lower plot b) $100 \cdot 2\pi$ MHz. The probe laser is continuous wave and the coupling laser pulsed, whereby a rectangular pulseshape and duration of 10 ns is assumed. The gray dashed lines mark the beginning and end of the pulse.

11 Experimental Results

11.1 Resonant GHz Rabi Flopping

When measuring signals on the nanosecond timescale, the properties of the used devices play an important role, as e.g. the bandwidth of the coaxial cables and oscilloscope must be higher than the frequency of the measured signal. Also the finite travel speed of light and electronic signals can not be neglected any more as 1 m equals a time delay of roughly 3 ns. As shown in fig. 9.1 two different photodiodes are used to measure the coupling pulse and the probe transmission, resulting in a time difference between those signals, which has to be deducted manually. In the top of fig. 11.1 both signals are shown with the adjusted offset. The gray dashed lines mark the beginning and end of the pulse, which is defined as the point on the rising or falling slope at which the mean value changes the most, resulting in a pulse length of 10.65 ns. Here it is to note that as stated in section 5.2.1 the slow decay after the pulse is an effect caused by the photodiode as the actual pulse goes back to zero. As a first response to the coupling laser the probe transmission increases slightly before decreasing and uniform oscillations can be observed. This first increase, which could not be observed in the simulations in fig. 10.2, can be attributed to the rise time of the coupling pulse, which is not, as assumed in the simulations, infinitesimally small. With the end of the pulse, the probe transmission drops abruptly due to the fast decrease of the coupling Rabi frequency. The number of atoms remaining in the Rydberg state depends on the the exact point in the Rabi cycle where the pulse stops. Those atoms then slowly decay back into the ground state, either by direct/indirect decays or because the fly out of the probe area. In the probe transmission signal it can also be seen that the two level system between ground and intermediate states approaches the steady state solution again, whereby the timescale of this is given by the different decays from the intermediate to the ground state and can be determined by fitting the function of an exponential decay to the they tail of the transmission after the coupling pulse (shown as black dashed line in fig. 11.1. The obtained lifetime and resulting decay rate are

$$\tau_{\text{meas}} = 30.85(19)\,\text{ns} \tag{11.1}$$

$$\gamma_{\text{meas}} = 32.42(20) \cdot 10^6\,\frac{1}{\text{s}}. \tag{11.2}$$

The effective lifetime of the $6P_{1/2}$ state consists of two parts, the natural lifetime with $\tau_0 = 129.29\,\text{ns}$ (calculated using [23]) which equals $\gamma_0 = 7.735 \cdot 10^6\,\frac{1}{\text{s}}$ and the transit

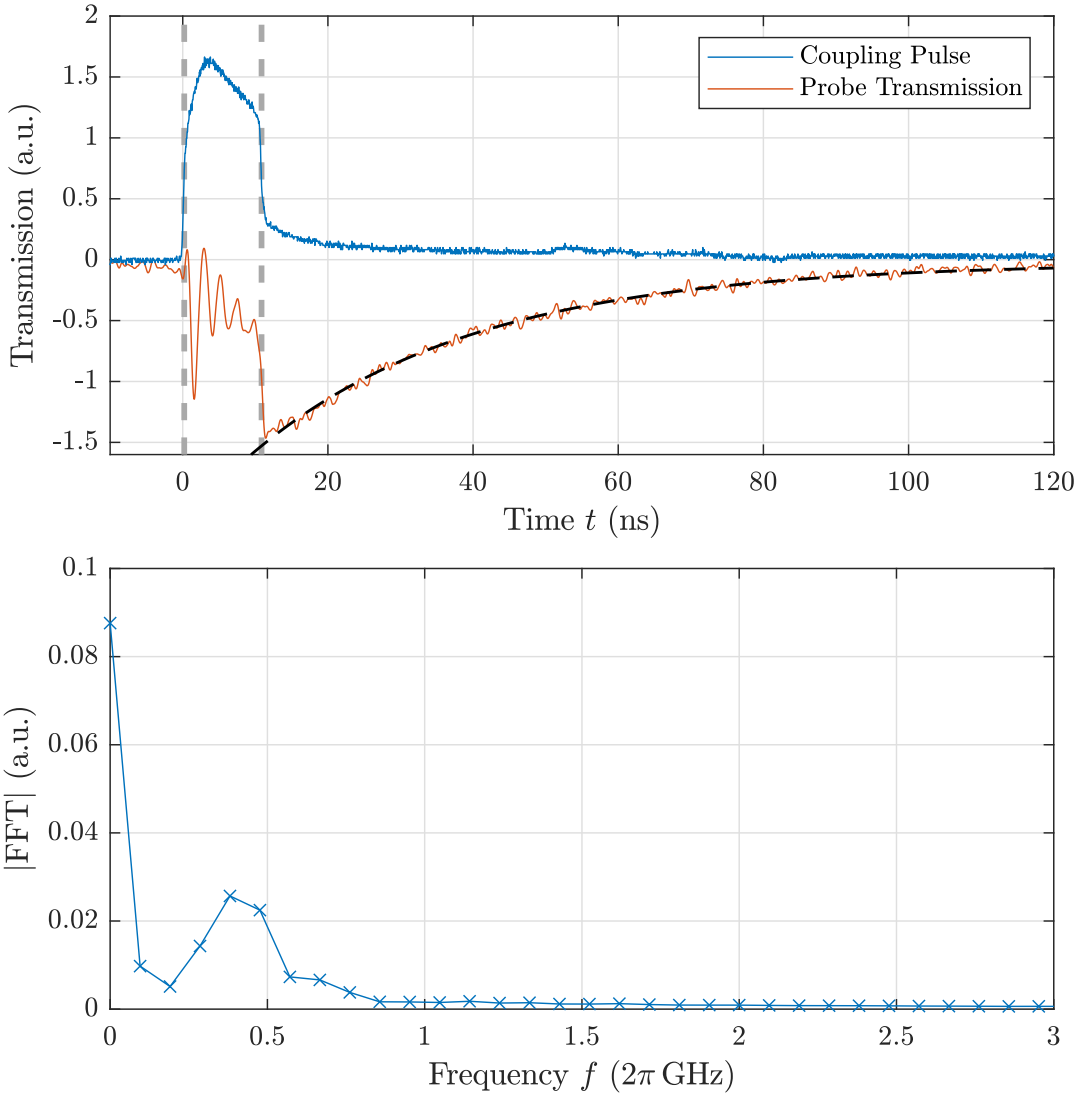

Figure 11.1: Top: In blue the coupling pulse is shown and in red the temporal probe transmission signal. The gray dashed lines mark the beginning and end of the pulse (definition in text). The corresponding Rabi frequencies are $\Omega_{422} = 15.82 \cdot 2\pi\,\mathrm{MHz}$ and $\Omega_{1016} = 1315.22 \cdot 2\pi\,\mathrm{MHz}$ for the probe and coupling transition. Bottom: Fourier transformation of the oscillating probe transmission signal in the time window of the coupling pulse (gray dashed lines).

time. The transit time rate can be estimated using eq. (1.50)

$$\gamma_{tt} = 16.23 \cdot 10^6 \, \frac{1}{\mathrm{s}} \tag{11.3}$$

compared to the value obtained from the measurement

$$\begin{aligned} \gamma_{tt,\mathrm{meas}} &= \gamma_{\mathrm{meas}} - \gamma_0 \\ &= 24.69 \cdot 10^6 \, \frac{1}{\mathrm{s}} \end{aligned} \tag{11.4}$$

the theoretical value is roughly 1.5 times smaller, but as previously stated eq. (1.50) is only an estimation for the order of magnitude of the value and does not give exact values.
In order to determine the oscillation frequency of the measured Rabi oscillations the probe signal in the corresponding time window is Fourier transformed which can be seen in the bottom of fig. 11.1. The oscillation frequency corresponds to the visible peak at a frequency of $381(95) \cdot 2\pi\,\mathrm{MHz}$. In theory this should equal half the coupling Rabi frequency $658(11) \cdot 2\pi\,\mathrm{MHz}$. In comparison the measured value is significantly smaller than the theoretical, meaning the actual Rabi frequency of the coupling laser is smaller than calculated. This can be attributed to two different things, either the laser power was smaller than assumed or the beam waist larger. One weakness of the setup of this experiment is that the cell has to be removed in order to overlap the two beams and perform the pinhole measurement. But when returning the cell, due to the dichroic properties of glass and the different propagation directions the position of the two foci changes. Due to the Gaussian profile of the two beams this could lead to the situation that the probing area is not at the maximum coupling frequency. In order to compensate this it is necessary to optimize the probe signal to achieve a maximum Rabi oscillation frequency. In the scope of this thesis, this was done by manually varying the in-coupling of the Rydberg laser. However, in this setup the necessary fine tuning was technically not possible. In order to improve the signal it is therefore necessary to have more control over the overlap of the two laser beams with e.g. motorized mirrors which can be remotely controlled to systematically optimize the signal.
By taking the values for the coupling Rabi frequency and transit time decay determined in the experiment as well as the measured pulse shape, those can be used in order to simulate the results like described in chapter 10. The result can be seen in fig. 11.2. For the coupling pulse (shown in blue) the measured pulseshape was slightly modified by cutting of the slow decay after the actual pulse, which is caused by a glitch of the photodiode. Also a peak Rabi frequency of $900 \cdot 2\pi\,\mathrm{MHz}$ is assumed which corresponds to an average Rabi frequency of $750 \cdot 2\pi\,\mathrm{MHz}$ during the duration of the pulse. The probe Rabi frequency is also the same as in the experiment with 15.82 MHz. All decay rates can be found in appendix B. When directly comparing experiment and simulation figs. 11.1 and 11.2 a few things can be noted. First of all the assumption, that the initial

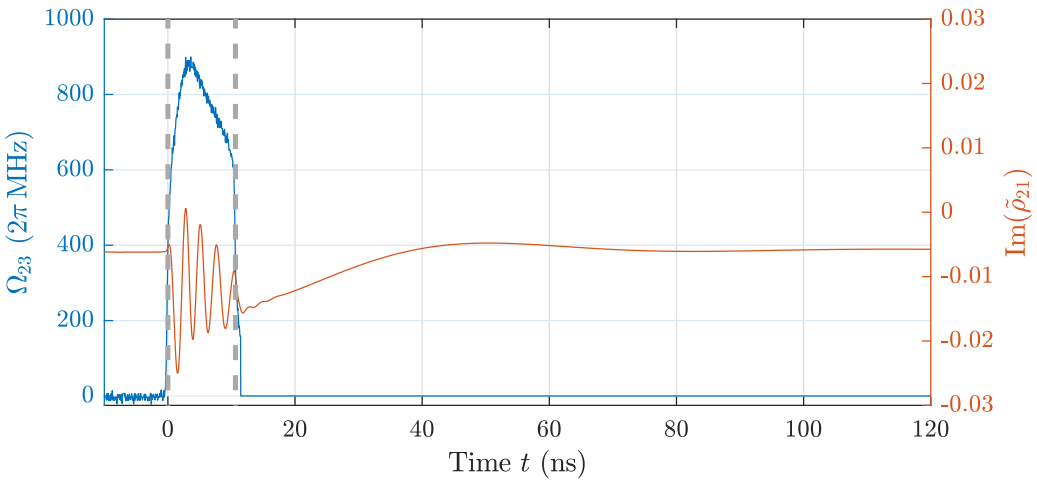

Figure 11.2: Simulated coherences $\mathrm{Im}(\tilde{\rho}_{21})$ for a three level system of the $5S_{1/2} \rightarrow 6P_{1/2} \rightarrow 32S_{1/2}$ transition with counter propagating laser beams, the corresponding decays (see appendix B) and a temperature of 155 °C. In blue the pulse shape of the coupling Rabi frequency Ω_{23} is shown with a peak frequency of $900 \cdot 2\pi$ MHz the pulseshape is adapted from the experimental measurement where the glitch after the pulse caused by the photodiode is removed. The probe laser is continuous waved with a Rabi frequency of $15.82 \cdot 2\pi$ MHz

increase of the signal once the pulse arrives is due to the finite rise time of the coupling pulse can be confirmed, as this peak was not visible in the simulations in chapter 10, with a perfect rectangular pulse, but is visible in this simulation using the actual pulseshape. Furthermore, the frequency of the oscillations match nicely due to the equal coupling Rabi frequencies. But a difference can be seen in the amplitude of the oscillations. In both cases the maximum amplitude of each Rabi cycle decreases with time after the first oscillation, but in the experiment this is more significant. This behavior indicates that in the experiment additional decay or dephasing effects occur which are not included in the simulations, like collisions between the atoms. The sharp decrease of the signal after the pulse, as seen in the measurement, is also found in the simulation. However, the exact decay back into the steady state can not be reproduced, but as previously stated this depends heavily on the exact point of the Rabi oscillation at which the coupling pulse stops and the corresponding phase of the coherence at that moment. As both Rabi frequencies could not have been determined to the precision needed to reproduce this, the behavior of the measured probe transmission signal after the pulse could not be reproduce in the simulations.

As the presented measurement is done using an AC coupled photodiode, the information of the absolute value of the signal is lost. The advantage of the AC photodiode is however, that it is technically easier to amplify a signal with a certain frequency range, than the whole frequency spectrum which would be needed for a DC photodiode. Here, the additional amplification is needed in order to measure the Rydberg Rabi oscillations with low probe intensities. For higher probe powers the signal can also be detected using a DC photodiode without additional amplification.
The comparison between the AC- and DC- photodiode can be seen in the upper part of fig. 11.3. Both signals show the previously described features and as expected the signal-to-noise ratio is significantly higher for the AC-photodiode. This is both due to the additional amplifier, but also the limited bandwidth serves as a noise filter. The absolute value given by the DC-photodiode can be used to compare the relative drop of the signal to the simulation shown in the lower plot of fig. 11.3. The experimentally determined decrease from the steady state level to the first dip in the Rabi oscillation is $\approx 11\,\%$ and from the simulation $\approx 6\,\%$.
It can be concluded from this, that the presented simulation model is not only suitable for a qualitative description of the experiment, but also provides quantitative results in the correct order of magnitude. This is an important tool for the pulsed four wave mixing experiment later on, as e.g. the Rydberg population can be extracted from the simulation, which can not be easily measured.

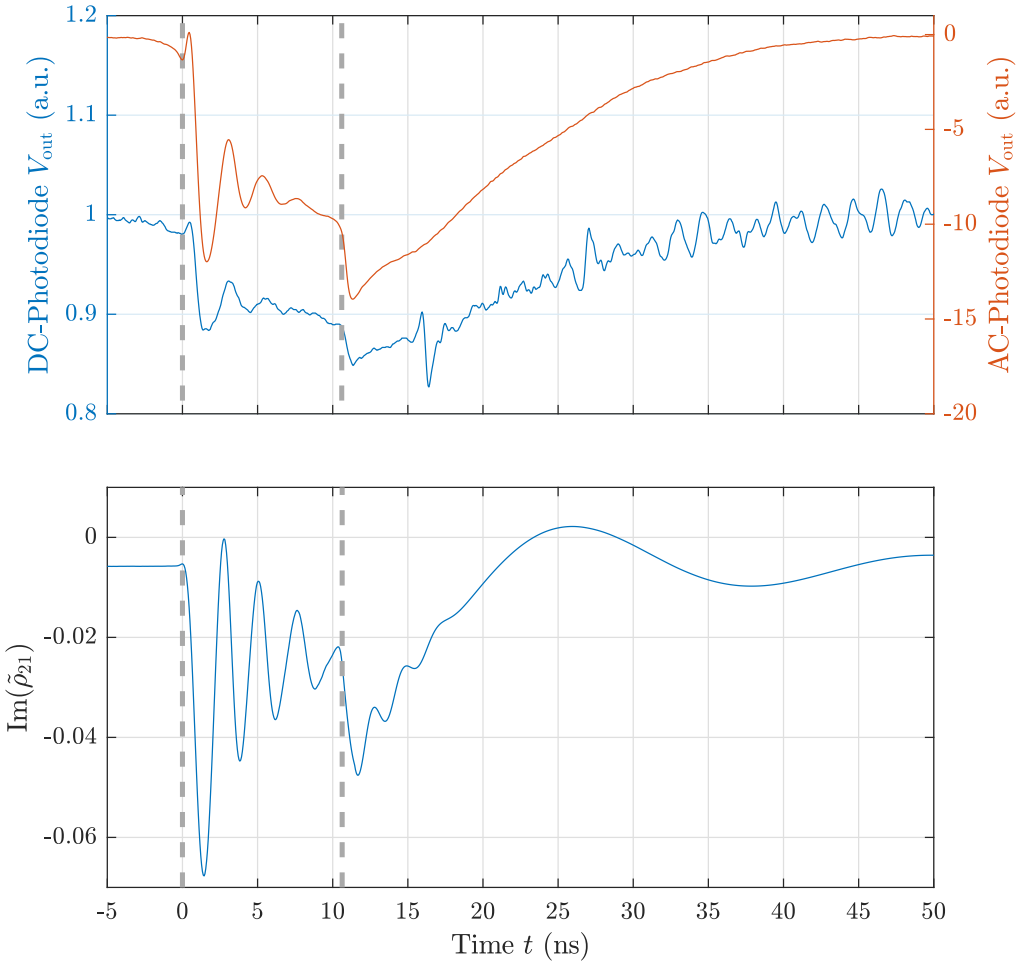

Figure 11.3: Top: Comparison of the measured output voltage V_{out} of an AC and DC coupled photodiode, with probe and coupling Rabi frequencies of $41.85 \cdot 2\pi$ MHz and $1315.22 \cdot 2\pi$ MHz respectively. Bottom: Corresponding simulation with the same probe Rabi frequency but coupling Rabi frequency of $900 \cdot 2\pi$ MHz.

11.2 Dependency on Rabi Frequency

In order to investigate the influence of the coupling Rabi frequency in more detail the probe transmission is measured for different powers of the Rydberg laser. As previously stated the effective Rabi frequency, corresponding to the oscillation frequency measured in the probe transmission is given by

$$\begin{aligned} \Omega_{\text{eff}} &= \frac{1}{2}\sqrt{\Omega_{422}^2 + \Omega_{1016}^2} \\ &\approx \frac{1}{2}\Omega_{422} \qquad\qquad \text{for } \Omega_{1016} \gg \Omega_{422} \end{aligned} \tag{11.5}$$

This means for high coupling and low probe Rabi frequencies, the dependency can be approximated as linear, whereas if the two Rabi frequencies are in the same order of magnitude the square root-like behavior is expected. The top part of fig. 11.4 shows the measurement results. For points of constant phase, e.g. the yellow lines regions indicating a peak in the oscillation cycle, the square-root behavior according to eq. (11.5) can be seen. The lower part of fig. 11.4 shows the according simulations. Similar to section 11.1 lower than calculated Rabi frequencies were used for this simulation, but an otherwise good agreement to the experiment can be found.

11.3 Detuning Dependency

All previously discussed formulas only account for resonant excitations. Therefore in this section the influence of an additional detuning for the Rydberg laser shall be investigated. Figure 11.5 shows the simulated coherence between ground and intermediate state for different detunings Δ_{23} of the coupling laser. It can be seen, that for increasing detunings the frequency of the Rabi oscillations decreases. This behavior contradicts the behavior of a simple two level system, in which the off resonant effective Rabi frequency is given by $\Omega_{\text{eff}} = \sqrt{\Omega^2 + \Delta^2}$ and thus increases with the detuning. This is due to an Autler-Townes splitting between the intermediate and Rydberg state, induced by the strong coupling pulse. Therefore, it is useful to transform the system in the dressed state picture, where the superposition of intermediate and Rydberg state form the new states $|+\rangle$ and $|-\rangle$ like derived in section 1.4.2 and the splitting between those is given by the coupling Rabi frequency.
In the case of atoms at rest and resonant excitation, the probed oscillation frequency is exactly half of the coupling Rabi frequency. With an increasing coupling detuning however, the distance from one of the dressed state to the ground state decreases while the other increases, depending on the sign of the detuning (see p.53, fig.4.9 in [30]). As the respective state gets closer to the ground state, the probed Rabi frequency decreases while for the other state moving away from the ground state, the Rabi frequency increases. As the population also increases for the state closer to the ground state, this

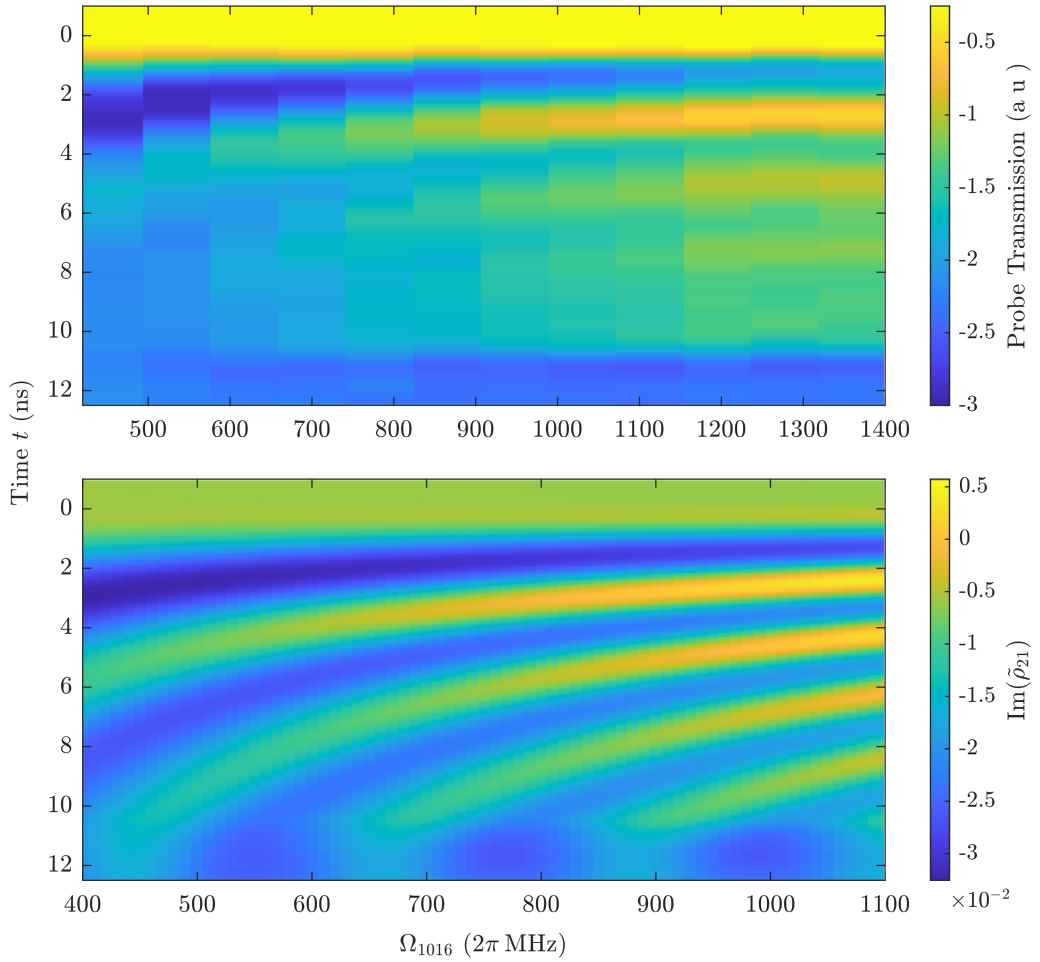

Figure 11.4: Top: Measured transmission of the probe laser in dependence of the peak coupling Rabi frequency. Bottom: Simulated transmission $\mathrm{Im}(\tilde{\rho}_{21})$ assumed decay rates can be found in appendix B for both cases $\Omega_{422} = 18.04 \cdot 2\pi\,\mathrm{MHz}$.

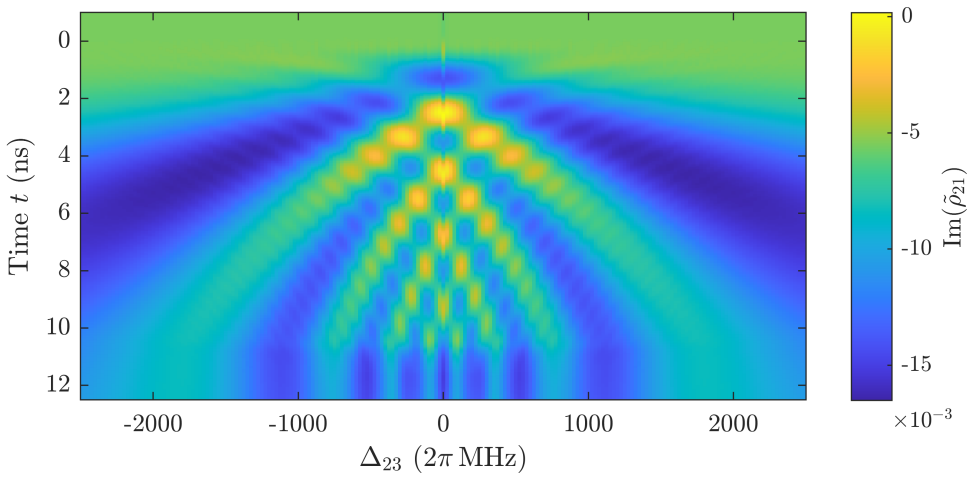

Figure 11.5: Simulation of the coherence between ground and intermediate state $\mathrm{Im}(\tilde{\rho}_{21})$ for different coupling detunings Δ_{23}, with a probe and coupling Rabi frequency of $10 \cdot 2\pi\,\mathrm{MHz}$ and $1000 \cdot 2\pi\,\mathrm{MHz}$ respectively.

signal with decreased Rabi frequency dominates.

For moving atoms the Doppler effect leads to an additional detuning, which means that for certain velocity classes the dressed states even approach resonance, leading to an even more prominent signal with slower oscillation. The average contribution from all velocity results in the signal shown in fig. 11.5
This however is, only a very simplified explanation and further discussion can be found in [8, 30, 31].

The data obtained from the measurement shown in fig. 11.6 however, does not match the simulation. The frequency axis was relatively scaled using a reference cavity and the absolute zero point corresponds to the on-resonance EIT signal observed in a reference cell using the reference continuous wave output of the fiber amplifier. In the detuning range between roughly $\pm 1000 \cdot 2\pi\,\mathrm{MHz}$, Rabi oscillations can be seen, which do not have the maximum frequency at $\Delta_{1016} = 0$ but rather at $1000 \cdot 2\pi\,\mathrm{MHz}$. For higher positive detunings comparably slow frequencies can be observed, further decreasing for higher detunings. This part matches quantitatively to the simulations.
For negative detunings on the other hand, the Rabi oscillations get slower until at $\approx -1900 \cdot 2\pi\,\mathrm{MHz}$ a regime is reached, where the coupling laser does not induce any measurable effect on the probe transition, and the signal stays constant. Decreasing the detuning more for $\Delta_{1016} < -2100 \cdot 2\pi\,\mathrm{MHz}$ the probe transmission decreases again during the pulse time. It can not be determined, whether this corresponds to a Rabi oscillation with a period longer than the pulselength or solely a decay.
In comparison, in [31] a similar experiment was done in the not inverted scheme and

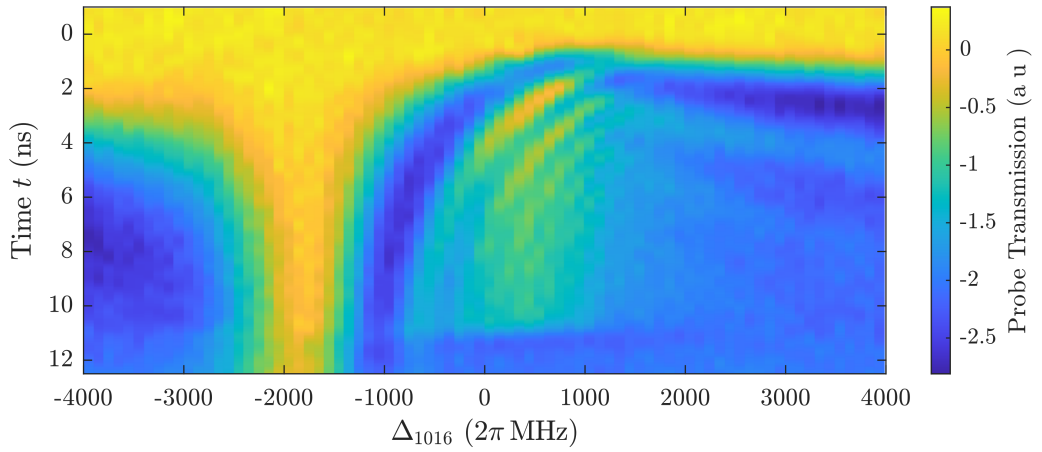

Figure 11.6: Measured probe transmission for different coupling detunings Δ_{1016}, with probe and coupling frequencies of $22.4 \cdot 2\pi$ MHz and $1357 \cdot 2\pi$ MHz respectively.

the $5P_{3/2}$ intermediate state, they also used the same simulation method, however, they present good agreement between measurement and simulation. Furthermore, the qualitative behavior matches the one observed in fig. 11.5.

The most puzzling part about the measurement results is, that it does not show any symmetry around the suspected resonance. This suggests, that this is not the perceived resonance from the perspective of atoms experiencing the pulse. As previously stated, this reference point was determined in a different reference cell using continuous wave spectroscopy with comparable weak Rabi frequencies.

An explanation of this effect therefore likely needs to include additional line shifts introduced by the excitation. One possibility is the AC-Stark shift [32]. Similar to the DC-Stark effect (see eq. (8.4)), a strong pulsed laser leads to a shift of all atomic levels. Depending on the field strength E of the pulsed laser and the dynamic polarizability $\alpha(\lambda)$, the shift can be approximated as

$$\delta_{\text{AC-Stark}} \approx -\frac{1}{4}\alpha(\lambda)\, E^2. \tag{11.6}$$

The dynamic polarizability of the ground state, induced by a light field with a wavelength of 1016 nm, can be calculated using [23], resulting in

$$\alpha(1016\,\text{nm}) = 1.90 \cdot 10^{-5}\, \frac{\text{Hz}}{(\text{V/m})^2}. \tag{11.7}$$

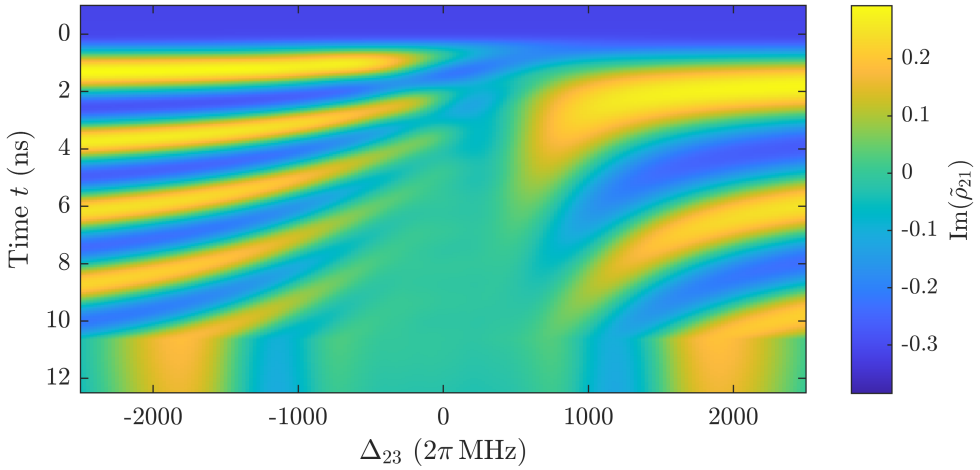

Figure 11.7: Simulation of the coherence between ground and intermediate state $\mathrm{Im}(\tilde{\rho}_{21})$ for different coupling detunings Δ_{23}, with a probe and coupling Rabi frequency of $10 \cdot 2\pi$ MHz and $1000 \cdot 2\pi$ MHz, including the AC-Stark shift of the ground state with $327 \cdot 2\pi$ MHz. In first approximation the AC-Stark shift is assumed to be constant during the coupling pulse and otherwise zero.

Assuming a peak power of 100 W and a beam waist of 37.35 μm this corresponds to an energy shift of

$$\delta_{\text{AC-Stark}} \approx -327 \cdot 2\pi \,\text{MHz}. \tag{11.8}$$

This can be included into the simulations as an additional time dependent detuning to the ground state and the result can be seen in fig. 11.7. Before and after the coupling pulse the Stark shift is estimated to be zero and assumed to be constant during the pulse. It can be seen, that the simulated coherence shows also a not symmetric behavior, with slower oscillations for positive detunings and faster oscillations for negative detunings. Apart from this the overall behavior is still not in good agreement with the experimental data. This indicates, that in the measurement additional effects occur. For example, it was neglected so far, that the Stark shift has an influence on the other energy levels, also the coupling laser could induce a ionization shift or broadening due to the creation of a plasma.

In order to investigate the detuning dependency of the signal further and understand the underlying theory, further measurements are required, like a systematic scan not only for the coupling detuning but also the probe detuning.

Conclusion and Outlook

In the course of this thesis systematic measurements were performed, investigating the two photon excitations to the Rydberg state in the inverted level scheme via the $6P_{1/2}$ intermediate state in rubidium.

Initial measurements were performed using continuous wave lasers. In the resulting steady state regime it was shown, that an Autler-Townes splitting can be induced as well as probed by the ground state laser using a probe Rabi frequency in the order of a few megahertz and a coupling Rabi frequency of around one megahertz. The absolute value of the Autler-Townes splitting was in good agreement with corresponding three-level steady state simulations.
For higher coupling Rabi frequencies (a few megahertz), electromagnetically induced transparency (EIT) could be observed for the two intermediate hyperfine states $6P_{1/2}$ $F' = 2$ and $F' = 3$. The effective separation between those transitions can be compared with the literature hyperfine splitting, if the wavelength ratio is respected. This was done for co- and counter-propagating laser configurations and in both cases good agreement to the literature was found.
Furthermore, for decreasing probe Rabi frequency with counter-propagating lasers a transition between induced transmission and induced absorption was observed. This is attributed to an additional, dominant dephasing, which suppresses the phase sensitive EIT-process in contrast to the non-phase sensitive enhanced absorption. Other shifts and broadenings, that might be attributed to the creation of a plasma were observed and discussed.

In the second part of this thesis, a customized fiber amplifier was used to create nanosecond pulses with a peak power of up to 100 W in order to excite the Rydberg transition. By focusing the coupling laser to a focal waist below 50 μm, Rabi frequencies of up to one gigahertz could be reached. These Rabi oscillations were directly detected by measuring the probe transmission signal, proving that fully coherent dynamics can be achieved on the nanosecond timescale. The dynamics of the system and its behavior for different coupling Rabi frequencies are in good agreement with simulations of a three-level system.
However, detuning dependent measurements could not be reproduced in the same fashion. This implies additional effects inducing a line shift, which are not included in the simulations. Possible explanations include the formation of a plasma, similar to the continuous wave case.

To determine the origin of these effects and to further understand the underlying processes in this pulsed scheme, additional systematic measurements are required. This could include a variation of both laser detunings, or extended power scans.

Once the two-photon process is understood it will pave the way towards the realization of the single-photon source in the new excitation scheme. After adding the second Rydberg laser the full four-wave-mixing process can be explored.

Appendix

A Rubidium Level Scheme

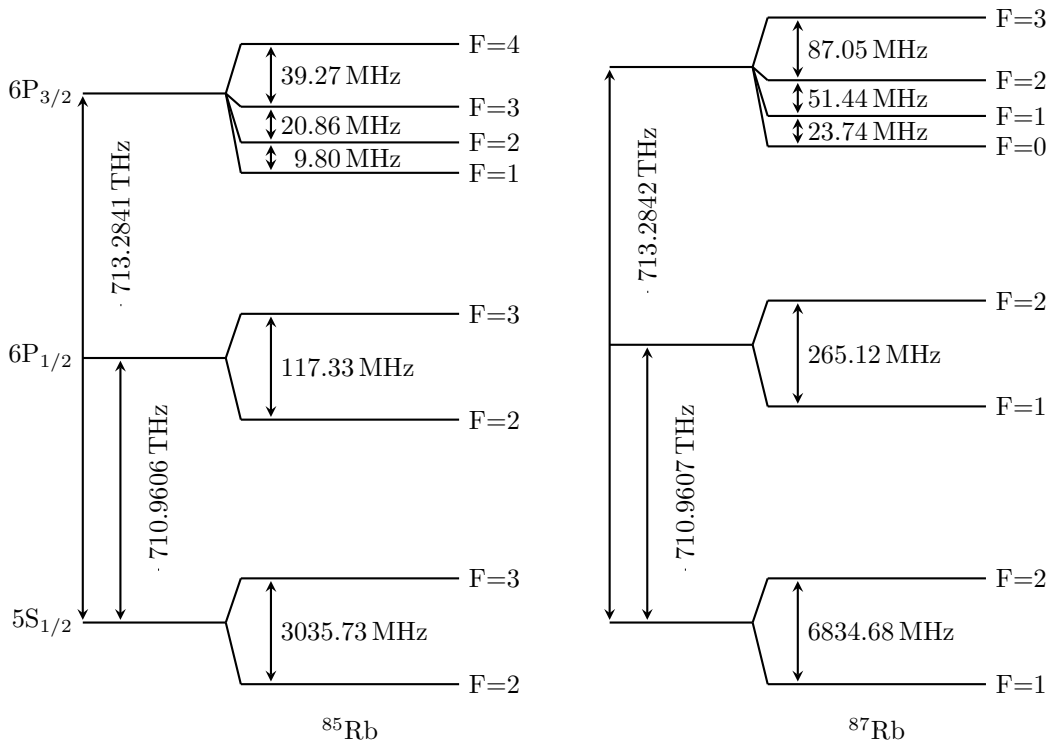

Figure A.1: Level scheme of ^{85}Rb and ^{87}Rb for the $5S_{1/2}$, $6P_{1/2}$ and $6P_{3/2}$ states including the hyperfine splittings. All values are given in units of 2π and taken from [22]. Drawing not to scale.

B Decay Rates

The following decay rates were used for all simulations including the corresponding rubidium states.

Table B.1: Lifetime and corresponding decay rates for selected rubidium states calculated using [23]

state	lifetime (s)	decay rate $\left(\frac{1}{\mathrm{s}}\right)$
$6\mathrm{P}_{1/2}$	$1.29 \cdot 10^{-7}$	$7.73 \cdot 10^{6}$
$6\mathrm{P}_{3/2}$	$1.18 \cdot 10^{-7}$	$8.46 \cdot 10^{6}$
$32\mathrm{S}_{1/2}$	$3.01 \cdot 10^{-5}$	$3.32 \cdot 10^{4}$
$32\mathrm{S}_{1/2}$	$6.27 \cdot 10^{-5}$	$1.59 \cdot 10^{4}$

Table B.2: Decay rates between specific rubidium states calculated using [23]

transition	decay rate $\left(\frac{1}{\mathrm{s}}\right)$
$6\mathrm{P}_{1/2} \rightarrow 5\mathrm{S}_{1/2}$	$1.498 \cdot 10^{6}$
$32\mathrm{S}_{1/2} \rightarrow 6\mathrm{P}_{1/2}$	$2.11 \cdot 10^{3}$
$40\mathrm{S}_{1/2} \rightarrow 6\mathrm{P}_{1/2}$	$1.01 \cdot 10^{3}$

Bibliography

[1] E. Knill, R. Laflamme, and G. A. Milburn, "A scheme for efficient quantum computation with linear optics," vol. 409, pp. 46–52, jul 2000.

[2] P. Michler, A. Kiraz, C. Becher, W. V. Schoenfeld, P. M. Petroff, L. Zhang, E. Hu, and A. Imamoglu, "A quantum dot single-photon turnstile device," *Science*, vol. 290, no. 5500, pp. 2282–2285, 2000.

[3] C. Kurtsiefer, S. Mayer, P. Zarda, and H. Weinfurter, "Stable solid-state source of single photons," *Phys. Rev. Lett.*, vol. 85, pp. 290–293, Jul 2000.

[4] T. F. Gallagher, "Rydberg atoms," *Reports on Progress in Physics*, vol. 51, pp. 143–188, February 1988.

[5] M. D. Lukin, M. Fleischhauer, R. Cote, L. M. Duan, D. Jaksch, J. I. Cirac, and P. Zoller, "Dipole blockade and quantum information processing in mesoscopic atomic ensembles," *Phys. Rev. Lett.*, vol. 87, p. 037901, Jun 2001.

[6] F. Ripka, H. Kübler, R. Löw, and T. Pfau, "A room-temperature single-photon source based on strongly interacting rydberg atoms," *Science*, vol. 362, no. 6413, pp. 446–449, 2018.

[7] O. de Vries, M. Plötner, F. Christaller, H. Zhang, A. Belz, B. Heinrich, H. Kübler, R. Löw, T. Pfau, T. Walbaum, T. Schreiber, and A. Tünnermann, "Highly customized 1010 nm, ns-pulsed yb-doped fiber amplifier as a key tool for on-demand single-photon generation," *Opt. Express*, vol. 28, pp. 17362–17373, Jun 2020.

[8] T. Baluktsian, *Rydberg interaction between thermal atoms: Van der Waals-type Rydberg-Rydberg interaction in a vapor cell experiment*. PhD thesis Universität Stuttgart, 2013.

[9] F. Ripka, *Creation of non-classical light in a thermal μ-cell*. PhD thesis Universität Stuttgart, 2019.

[10] C. Carr, *Cooperative Non-Equilibrium Dynamics in a Thermal Rydberg Ensemble*. Durham theses, Durham University. Available at Durham E-Thesis Online: `http://etheses.dur.ac.uk/8450/`, 2019.

[11] D. A. Steck, *Quantum and Atom Optics*. aviable online at `http://steck.us/teaching` (revision 0.13.4,24 September 2020), 2007.

[12] G. Lindblad, "On the generators of quantum dynamical semigroups," *Communications in Mathematical Physics*, vol. 48, pp. 119–130, Jun 1976.

[13] D. A. Steck, *Rubidium 85 D Line Data*. aviable online at `http://www.steck.us/alkalidata` (revision 2.2.2, 29 April 2021), 2008.

[14] P. M. Anisimov, J. P. Dowling, and B. C. Sanders, "Objectively discerning autler-townes splitting from electromagnetically induced transparency," *Phys. Rev. Lett.*, vol. 107, p. 163604, Oct 2011.

[15] W. Li, I. Mourachko, M. W. Noel, and T. F. Gallagher, "Millimeter-wave spectroscopy of cold rb rydberg atoms in a magneto-optical trap: Quantum defects of the ns, np, and nd series," *Phys. Rev. A*, vol. 67, p. 052502, May 2003.

[16] Y.-Y. Jau, A. M. Hankin, T. Keating, I. H. Deutsch, and G. W. Biedermann, "Entangling atomic spins with a rydberg-dressed spin-flip blockade," *Nature Physics*, vol. 12, pp. 71–74, October 2015.

[17] D. A. Steck, *Rubidium 87 D Line Data*. aviable online at `http://www.steck.us/alkalidata` (revision 2.2.1, 21 November 2019), 2001.

[18] E. D. Black, "An introduction to pound–drever–hall laser frequency stabilization," *American Journal of Physics*, vol. 69, no. 1, pp. 79–87, 2001.

[19] A. Cygan, D. Lisak, P. Masłowski, K. Bielska, S. Wójtewicz, J. Domyslawska, R. Trawiński, R. Ciuryło, H. Abe, and J. Hodges, "Pound-drever-hall-locked, frequency-stabilized cavity ring-down spectrometer," *The Review of scientific instruments*, vol. 82, p. 063107, 06 2011.

[20] H. Kogelnik and T. Li, "Laser beams and resonators," *Appl. Opt.*, vol. 5, pp. 1550–1567, Oct 1966.

[21] M. Seltenreich, *Eigenschaften eines digitalen, vielseitigen und erweiterbaren Systems zur Laserfrequenzstabilisierung*. Bachelor thesis Universität Stuttgart, 2021.

[22] C. Glaser, F. Karlewski, J. Kluge, J. Grimmel, M. Kaiser, A. Günther, H. Hattermann, M. Krutzik, and J. Fortágh, "Absolute frequency measurement of rubidium $5s-6p$ transitions," *Phys. Rev. A*, vol. 102, p. 012804, Jul 2020.

[23] N. Šibalić, J. Pritchard, C. Adams, and K. Weatherill, "Arc: An open-source library for calculating properties of alkali rydberg atoms," *Computer Physics Communications*, vol. 220, pp. 319–331, 2017.

[24] A. Urvoy, C. Carr, R. Ritter, C. S. Adams, K. J. Weatherill, and R. Löw, "Optical coherences and wavelength mismatch in ladder systems," *Journal of Physics B: Atomic, Molecular and Optical Physics*, vol. 46, p. 245001, nov 2013.

[25] B. K. Teo, D. Feldbaum, T. Cubel, J. R. Guest, P. R. Berman, and G. Raithel, "Autler-townes spectroscopy of the $5S_{1/2}-5p_{3/2}-44d$ cascade of cold ^{85}Rb atoms," *Phys. Rev. A*, vol. 68, p. 053407, Nov 2003.

[26] I. Hertel and C. Schulz, *Atome, Moleküle und optische Physik 1: Atomphysik und Grundlagen der Spektroskopie*. Springer-Lehrbuch, Springer Berlin Heidelberg, 2015.

[27] D. Weller, J. P. Shaffer, T. Pfau, R. Löw, and H. Kübler, "Interplay between thermal rydberg gases and plasmas," *Physical Review A*, vol. 99, Apr 2019.

[28] C. Foot, *Atomic Physics*. Oxford Master Series in Physics, OUP Oxford, 2005.

[29] T. Baluktsian, B. Huber, R. Löw, and T. Pfau, "Evidence for strong van der waals type rydberg-rydberg interaction in a thermal vapor," *Phys. Rev. Lett.*, vol. 110, p. 123001, Mar 2013.

[30] B. Huber, *Coherent Rydberg dynamics and interaction above room temperature: The frozen gas regime and beyond*. PhD thesis Universität Stuttgart, 2014.

[31] B. Huber, T. Baluktsian, M. Schlagmüller, A. Kölle, H. Kübler, R. Löw, and T. Pfau, "Ghz rabi flopping to rydberg states in hot atomic vapor cells," *Phys. Rev. Lett.*, vol. 107, p. 243001, Dec 2011.

[32] N. B. Delone and V. P. Krainov, "AC stark shift of atomic energy levels," *Physics-Uspekhi*, vol. 42, pp. 669–687, jul 1999.

Danksagung

Zunächst möchte ich mich bei Prof. Dr. Tilman Pfau für die Möglichkeit bedanken, meine Masterarbeit am 5. physikalischen Institut durchzuführen.

Des Weiteren danke ich Prof. Dr. Hidenori Takagi für die Übernahme des Mitberichts und hilfreiche Diskussionen.

Zudem danke ich Robert Löw und Harald Kübler für ihre Anregungen und Unterstützung bei der Interpretation von Messergebnissen.

Es ist nicht selbstverständlich Betreuer zu haben, die bereit sind ausnahmslos alle Fragen zu beantworten und bei jeglichen Problemen im Labor zu helfen. Daher danke ich Max Mäusezahl und Florian Christaller für ihre Unterstützung und das Korrekturlesen dieser Arbeit.

Des Weiteren danke ich Felix Moumtsilis für die unermüdliche Hilfe im Labor und Apfeltaschen, die so manche lange Tage erträglicher gemacht haben.

Patrick Kaspar und Fabian Munkes danke ich für die Unterstützung und gute Zusammenarbeit bei dem Aufbau des Laser-Lock-Setups, sowie der gemeinsamen Bewältigung der dabei aufgekommenen Probleme.
Ebenfalls danke ich den restlichen Institutsmitgliedern für die große Hilfsbereitschaft und stets angenehme Arbeitsatmosphäre.

Außerdem danke ich Felix Roser, ohne den ich nicht einmal das erste Semester überstanden hätte, Janice Pelzer für die moralische Unterstützung vor allem in den letzten Monaten dieser Arbeit und Julia Greulich für den Beistand in jeglicher Situation.

Zuletzt möchte ich mich bei meiner Familie für die Unterstützung während meines Studiums bedanken, ohne welche dies nicht möglich gewesen wäre.